

1 **Numerical integration of an elasto-plastic critical state model for soils**
2 **under unsaturated conditions**

3 Author 1

- 4 • Martí Lloret-Cabot, Ph.D
- 5 Assistant Professor of Civil and Environmental Engineering
- 6 Department of Engineering
- 7 Durham University
- 8 UK

9 Author 2

- 10 • Simon J. Wheeler, Professor
- 11 Cormack Professor of Civil Engineering
- 12 James Watt School of Engineering
- 13 University of Glasgow
- 14 UK

15 Author 3

- 16 • Antonio Gens, Professor
- 17 Professor of Civil Engineering
- 18 Department of Civil and Environmental Engineering
- 19 Universitat Politècnica de Catalunya - CIMNE
- 20 Spain

21 Author 4

- 22 • Scott W. Sloan, Laureate Professor†
- 23 Professor of Civil Engineering
- 24 Priority Research Centre for Geotechnical Science and Engineering
- 25 The University of Newcastle
- 26 Australia.

27 †Laureate Professor Scott Sloan passed away unexpectedly during the preparation of this paper. The authors dedicate this work
28 to his memory

29

30 ABSTRACT

31 This paper presents the complete set of incremental equations for the numerical
32 integration of the Glasgow Coupled Model (GCM) and a comprehensive algorithm for
33 its numerical integration. The incremental formulation proposed is expressed in terms
34 of strain and suction increments (i.e. strain-driven) and defines an initial value problem
35 (IVP) that can be solved once the initial state and the pair of increments of the driven
36 variables are known. The numerical integration of this IVP is carried out by extending
37 to unsaturated condition, the well-known explicit substepping formulation with
38 automatic error control widely used for saturated soils. A notable feature of the
39 substepping integration scheme presented is that it integrates simultaneously the model
40 equations for both mechanical and water retention responses. Hence, the estimate of the
41 local truncation error to automatically adjust the size of the integration step is not only
42 affected by the local error in stresses and mechanical hardening parameter (as in a
43 saturated soil model) but, additionally, by the local error incurred in the integration of
44 the water retention relations (i.e. degree of saturation and water retention hardening
45 parameter). The correctness of the integration scheme is then verified by comparison
46 of computational outcomes against analytical/reference solutions.

47

48

49

50 1. INTRODUCTION

51 Advanced numerical methods have been applied to geomechanics during the last
52 decades to solve geotechnical problems involving unsaturated soils (e.g. Pinyol et al.,
53 2008, Borja and White, 2010, Cattaneo et al., 2014, Sheng et al., 2003ab, Gens, 2010,
54 Khalili et al., 2008, Ng et al., 2000, Nuth and Laloui, 2008, Tsiamposi et al., 2013,
55 Zhou and Sheng, 2015, Zhang et al., 2019). A key aspect in many of these numerical
56 applications is the amount of water retained in the soil pores because it controls the loss
57 or gain of soil's strength, critical to geotechnical instabilities. When the soil reaches full
58 saturation after intense rainfall, for instance, all the additional contribution of the
59 unsaturated condition to the soil strength vanishes. Changes in the saturation of the soil
60 are also relevant to serviceability design because substantial volumetric compressions
61 may occur during wetting (collapse) or drying (shrinkage) (Alonso et al., 1990,
62 Gallipoli et al., 2003, Lloret-Cabot et al., 2014).

63 The amount of water stored within the pores of a soil is described by the water retention
64 behaviour which relates the degree of saturation S_r (or the water content w) to matric
65 suction s (where s is the difference between pore air pressure u_a and pore water pressure
66 u_w). However, due to the occurrence of hysteresis, a one-to-one relation between S_r and
67 s is rarely observed in soils (Romero et al., 1999, Tarantino 2009, Wheeler et al., 2003).
68 In addition to this hysteresis, the water retention behaviour can be highly dependent on
69 changes of the soil's porosity and, hence, on the mechanical behaviour (Romero et al.,
70 1999, Tarantino 2009, Wheeler et al., 2003).

71 In order to represent accurately the potential changes in saturation when a soil is
72 subjected to external environmental actions it is necessary to use a model that properly
73 handles not only retention hysteresis but also the couplings between the mechanical
74 behaviour and the water retention response. A model that includes all these effects is
75 the Glasgow Coupled Model GCM (Wheeler et al., 2003; Lloret-Cabot et al., 2013),
76 and the major focus of this paper is the development of an integration scheme capable
77 to integrate, accurately and efficiently, the incremental constitutive relations of this
78 model.

79 The explicit substepping formulation with automatic error control proposed in Sloan,
80 (1987) and Sloan et al. (2001) has been extensively used in the literature for the
81 numerical integration of elasto-plastic models for saturated soils (Sloan et al., 2001,
82 Abbo, 1997, Sheng et al., 2000, Pedroso et al., 2008, Zhao et al., 2005, Pérez-Foguet et

83 al., 2001). Full extension of this formulation to the unsaturated case is presented in this
84 paper in the context of the GCM. The extended substepping integration scheme
85 integrates simultaneously the model equations for both mechanical and water retention
86 responses. Hence, the local error incurred during the numerical integration of the model
87 is not only affected by the local error in stresses and mechanical hardening parameters
88 (as in the saturated case) but, additionally, by the local error incurred in the integration
89 of the water retention relations. A consequence of this is that the measure of the local
90 error used in a substepping integration scheme to adjust automatically the size of the
91 next integration step is now estimated accounting for both sources of numerical error,
92 including the inexact integration of the mechanical and water retention relations.
93 Equivalent conclusions are reached when integrating other coupled constitutive models
94 for unsaturated soils with substepping integration schemes with automatic error control
95 (Zhang and Zhou, 2016).

96 The paper presents a comprehensive algorithm for the numerical integration of the
97 GCM. Although some aspects of the algorithm are linked to specific features of the
98 GCM, the overall approach is general and can be applied to other coupled constitutive
99 models for unsaturated soils.

100 A small reformulation of the GCM is first presented with the aim of simplifying its
101 numerical integration. Based on this reformulation, the relevant incremental
102 mechanical and water retention relations of the model for each possible response,
103 including unsaturated and saturated conditions, are developed. Two explicit
104 substepping integration schemes with automatic error control are proposed in order to
105 investigate the accuracy of the numerical integration: the second order modified Euler
106 with substepping and the fifth order Runge-Kutta-Dormand-Prince with substepping.
107 A verification study is presented at the end of the paper extending to unsaturated
108 conditions, the verification strategy proposed in Lloret-Cabot et al. (2016) for saturated
109 soils.

110 2. REFORMULATING GCM

111 Certain aspects of the GCM are reformulated in this section with the aim of simplifying
112 its numerical integration. This reformulation does not involve any modification of the
113 model, simply a change in how it is presented.

114 The version of the GCM presented here is that given in Lloret-Cabot et al. (2017), which
 115 assumes that there are no elastic changes of degree of saturation (the gradient of elastic
 116 scanning curves in the water retention plane is zero i.e. $\kappa_s = 0$ in the original model of
 117 Wheeler et al., 2003), in order to achieve consistent behaviour across transitions
 118 between unsaturated and saturated states.
 119 Soil mechanics sign convention is adopted hereafter (compression positive). Vectors
 120 and tensors are indicated in bold and the superscript T indicates transposed.

121 2.1. Mechanical Behaviour

122 The mechanical behaviour describes the stress-strain relations. In the GCM, strains are
 123 related to the ‘‘Bishop’s stress’’ tensor $\boldsymbol{\sigma}^*$, defined as:

$$124 \quad \boldsymbol{\sigma}^* = \boldsymbol{\sigma} - \mathbf{m}^T (S_r u_w - (1 - S_r) u_a) = \bar{\boldsymbol{\sigma}} + \mathbf{m}^T S_r s \quad (1)$$

125 where $\boldsymbol{\sigma}$ is the total stress tensor, $\mathbf{m}^T = (1, 1, 1, 0, 0, 0)$ an auxiliary vector, S_r the degree
 126 of saturation, u_a the pore air pressure, u_w the pore water pressure, s matric suction and
 127 $\bar{\boldsymbol{\sigma}}$ net stress tensor ($\bar{\boldsymbol{\sigma}} = \boldsymbol{\sigma} - \mathbf{m}^T u_a$). Equation 1 reverts to the saturated effective stress
 128 tensor $\boldsymbol{\sigma}'$ (i.e. $\boldsymbol{\sigma}' = \boldsymbol{\sigma} - \mathbf{m}^T u_w$) when $S_r = 1$.

129 2.1.1 Elastic response

130 The incremental elastic relationship between Bishop’s stress and strains is given by:

$$131 \quad d\boldsymbol{\sigma}^* = \mathbf{D}_e d\boldsymbol{\varepsilon} \quad (2)$$

132 where d refers to an infinitesimal variation and \mathbf{D}_e is the elastic stiffness matrix:

$$133 \quad \mathbf{D}_e = \begin{pmatrix} K + \frac{4}{3}G & K - \frac{2}{3}G & K - \frac{2}{3}G & 0 & 0 & 0 \\ & K + \frac{4}{3}G & K - \frac{2}{3}G & 0 & 0 & 0 \\ & & K + \frac{4}{3}G & 0 & 0 & 0 \\ & & & G & 0 & 0 \\ & & & & G & 0 \\ & & & & & G \end{pmatrix} \quad (3)$$

134 K and G in Equation 3 are, respectively, the elastic tangential bulk and shear moduli
 135 defined as:

$$136 \quad K = \frac{dp^*}{d\varepsilon_v^e} = \frac{vp^*}{\kappa} \quad (4)$$

$$137 \quad G = \frac{dq}{3d\varepsilon_d^e} \quad (5)$$

138 where p^* is the mean Bishop's stress, q is the deviatoric stress, ε_v^e is the elastic
 139 volumetric strain, ε_d^e is the elastic deviatoric strain, v is the specific volume and κ is
 140 the gradient of a swelling line in the $v:\ln p^*$ plane. A variety of expressions are possible
 141 for G (Potts and Zdravkovic, 1999), but the simplest is to assume a constant value of
 142 shear modulus.

143 Given that $\boldsymbol{\sigma}^* = \boldsymbol{\sigma}'$ when $S_r = 1$, Equation 2 has the advantage of converging naturally
 144 to the conventional saturated elastic relations of the Modified Cam Clay model, MCC
 145 (Roscoe and Burland, 1968).

146 2.1.2. Mechanical yield curve

147 In order to reduce potential inaccuracies in the evaluation of the mechanical yield curve
 148 f_M , Sheng et al. (2000) propose that f_M is normalised against a stress parameter, so that
 149 its evaluation is not significantly influenced by the magnitude of stresses. Using the
 150 preconsolidation stress p_0^* (also referred to as the mechanical yield stress) as a
 151 normalising factor, the general expression for the mechanical yield curve of the GCM
 152 is (Lloret-Cabot et al., 2013):

$$153 \quad f_M = \frac{3J_2}{(p_0^*)^2} + M(\theta)^2 \left[\left(\frac{p^*}{p_0^*} \right)^2 - \frac{p^*}{p_0^*} \right] = 0 \quad (6)$$

154 where J_2 is the second invariant of the deviatoric stress tensor \mathbf{s} (i.e. $\mathbf{s} = \boldsymbol{\sigma}^* - \mathbf{m}^T p^*$) and
 155 $M(\theta)$ is a function of the Lode's angle θ describing the shape of the mechanical yield
 156 surface in the deviatoric plane (Potts and Gens, 1984). Available expressions for $M(\theta)$
 157 in the literature for saturated conditions (e.g. Potts and Gens, 1984, Potts and
 158 Zdravkovic, 1999, Sheng et al., 2000) can be readily incorporated to the unsaturated
 159 case. However, for simplicity, M is assumed constant herein. Then, for axisymmetric
 160 conditions, the mechanical yield curve becomes:

$$161 \quad f_M = \frac{q^2}{(p_0^*)^2} + M^2 \left[\left(\frac{p^*}{p_0^*} \right)^2 - \frac{p^*}{p_0^*} \right] = 0 \quad (7)$$

162 where M is the slope of the critical state line in the $q:p^*$ plane and q is the deviatoric
 163 stress i.e. $q^2 = 3J_2$.

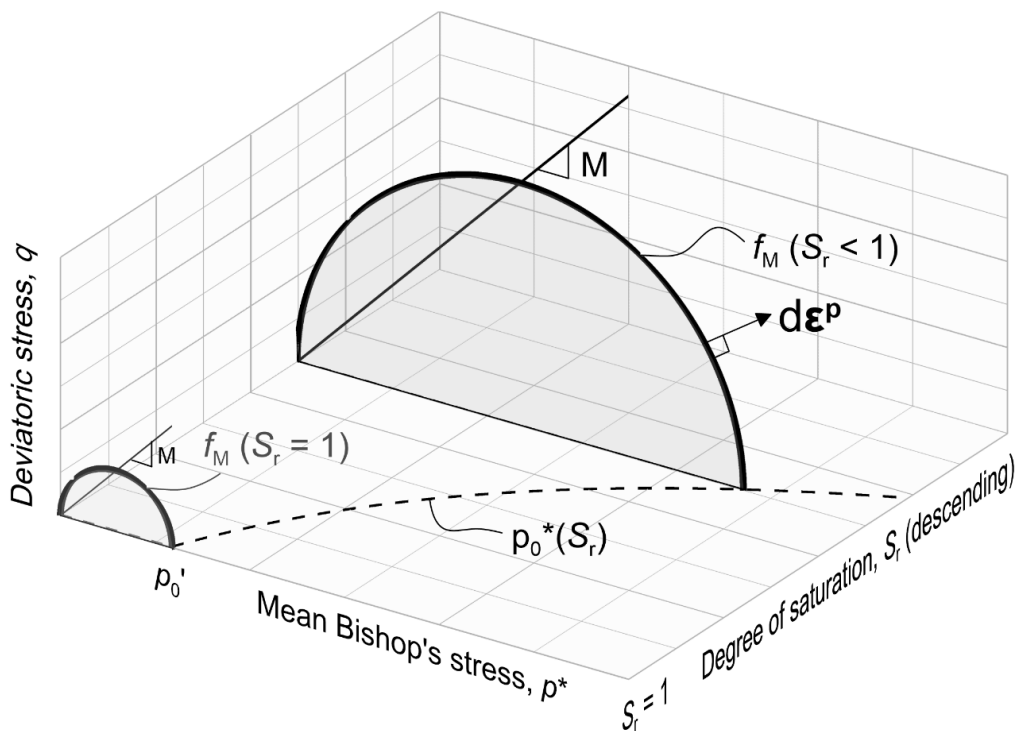
164 Expressions for $M(\theta)$ are possible by extending to the unsaturated case available
 165 expressions in the literature for saturated conditions (e.g. Potts and Gens, 1984, Potts
 166 and Zdravkovic, 1999, Sheng et al., 2000). For simplicity, axisymmetric conditions are
 167 assumed in the formulation presented here, so that M can be assumed a soil constant.

168 The preconsolidation stress p_0^* varies with the degree of saturation S_r according to:

$$169 \quad p_0^* = p_0' \exp\left(\frac{k_1}{\lambda_s}(1-S_r)\right) \quad (8)$$

170 where p_0' is the value of the saturated preconsolidation stress. k_1 and λ_s are soil
 171 constants.

172 Equation 6 indicates that the mechanical yield curve f_M is elliptical in shape (of aspect
 173 ratio M) when plotted in the $q:p^*$ plane (Figure 1). The size of this ellipse is defined by
 174 the current value of mechanical yield stress p_0^* , and this varies linearly with the degree
 175 of saturation in the $S_r: \ln p^*$ plane (Equation 8). For the special case of $S_r = 1$, the
 176 mechanical yield curve corresponds to the conventional ellipse of the MCC (Figure 1),
 177 because $p_0^* = p_0'$, which simplifies the implementation of the GCM in finite element
 178 programs where the MCC is already available.



179
 180 Figure 1 Typical mechanical yield curves of the GCM for a general value of S_r and for
 181 $S_r = 1$ in the $p^*:q:S_r$ space.

182 Interestingly, the new form of expressing the variations of mechanical yield stress with
 183 degree of saturation given by Equation 8 resembles the expression proposed by Jommi
 184 and Di Prisco (1994), with the difference here that the GCM represents the variation of
 185 degree of saturation within a single constitutive framework. Some of the advantages in
 186 constitutive modelling of expressing the mechanical (Bishop's) yield stress p'_0 in terms
 187 of degree of saturation are discussed in Lloret-Cabot & Wheeler (2018). Also, when
 188 the mechanical yield condition in GCM is represented in terms of Bishop's stresses and
 189 degree of saturation (as in Figure 1), there is no movement of the yield surface until the
 190 soil state reaches the surface. This contrasts with the original presentation of the GCM
 191 in Wheeler et al. (2003), where coupled movements of the mechanical yield surface
 192 (expressed there in terms of Bishop's stresses and modified suction s^* (defined later))
 193 occur during yielding on water retention yield surfaces. As a consequence, the new
 194 formulation has advantages in numerical modelling. Firstly, it is easier to use various
 195 common numerical techniques that have been developed to overcome issues arising
 196 when performing explicit numerical integration of saturated elasto-plastic critical state
 197 models (e.g. yield intersection, elasto-plastic unloading, drift correction, etc). Secondly,
 198 as demonstrated later, this specific form of f_M facilitates the formulation of an
 199 unambiguous strategy to identify the correct model response activated by any given
 200 stress path. Finally, it provides a very simple representation of the transitions between
 201 saturated and unsaturated conditions that avoids the drawbacks discussed in Pedroso et
 202 al. (2008) about the non-convex form of the mechanical yield curve at the transition
 203 from unsaturated to saturated states.

204 2.1.3. Hardening law

205 Given that the saturated preconsolidation stress p'_0 remains constant unless mechanical
 206 yielding occurs, it is possible to relate p'_0 to changes of plastic volumetric strains $d\varepsilon_v^p$
 207 through the following hardening law:

$$208 \frac{dp'_0}{p'_0} = \frac{v}{\lambda - \kappa} d\varepsilon_v^p \quad (9)$$

209 where κ is the gradient of a swelling line (in the $v:\ln p'$ plane for saturated conditions
 210 and the $v:\ln p^*$ plane for unsaturated conditions) and λ is the gradient of the saturated
 211 normal compression line in the $v:\ln p'$ plane.

212 Equation 9 is valid whether the soil is under saturated or unsaturated conditions and, as
 213 in the Barcelona Basic Model of Alonso et al. (1990), p'_0 can be viewed in the GCM as
 214 the mechanical hardening parameter. Equation 9 is identical to the conventional
 215 volumetric hardening law of the MCC which, as highlighted earlier, is helpful when
 216 combining existing critical state finite element formulations for saturated soils with the
 217 GCM.

218 2.1.4. Flow rule

219 An associated flow rule is adopted for the mechanical behaviour:

$$220 \quad d\boldsymbol{\varepsilon}^p = d\lambda_M \frac{\partial f_M}{\partial \boldsymbol{\sigma}^*} \quad (10)$$

221 where $d\lambda_M$ is an unknown positive scalar (referred to as the mechanical plastic
 222 multiplier) to be found by imposing that the stress point remains on f_M during
 223 mechanical yielding (consistency condition).

224 2.1.5. Analytical relations for the mechanical behaviour

225 The relationships for the mechanical behaviour of the GCM just presented lead to the
 226 following analytical expressions for isotropic normal compression states and critical
 227 states. These analytical expressions are relevant for verification purposes and provide
 228 further insight on specific features of the GCM. For example, isotropic stress states
 229 involving yielding on f_M are predicted to lie on a normal compression line in the $v:\ln p^*$
 230 plane, the position of which depends on the current value of S_r (see also Lloret-Cabot
 231 et al. 2018ab):

$$232 \quad v = N(S_r) - \lambda \ln p^* \quad (11)$$

233 where

$$234 \quad N(S_r) = N + \frac{k_1(\lambda - \kappa)(1 - S_r)}{\lambda_s} \quad (12)$$

235 and N is the intercept of the conventional saturated normal compression line (see Figure
 236 2).

237 Critical states, on the other hand, are defined by:

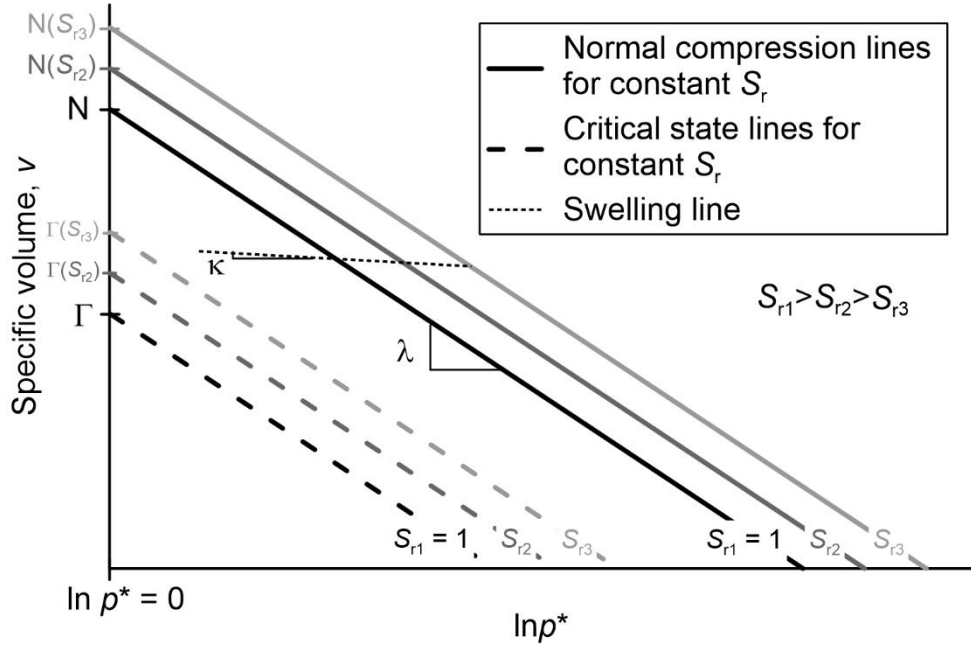
$$238 \quad q = Mp^* \quad (13)$$

$$239 \quad v = \Gamma(S_r) - \lambda \ln p^* \quad (14)$$

240 where q is the deviatoric stress and

$$241 \quad \Gamma(S_r) = N(S_r) - (\lambda - \kappa) \ln 2 = \Gamma + \frac{k_1 (\lambda - \kappa) (1 - S_r)}{\lambda_s} \quad (15)$$

242 and Γ is the intercept of the conventional saturated critical state line (see Figure 2).



243

244 Figure 2. Normal compression and critical state lines for constant values of S_r in the
245 $v:\ln p^*$ plane.

246 2.2. Water Retention Behaviour

247 Water retention behaviour is typically expressed in terms of degree of saturation S_r and
248 matric suction s , however, based on the work of Houlsby (1997), the GCM relates S_r to
249 the “modified suction” s^* , defined as:

$$250 \quad s^* = n(u_a - u_w) = \frac{v-1}{v} s \quad (16)$$

251 where n is porosity.

252 2.2.1. Elastic response

253 For situations where the GCM is to be used for both unsaturated and saturated
254 conditions, Lloret-Cabot et al. (2017) recommends to assume that elastic variations of
255 degree of saturation are zero $dS_r^e = 0$ (the gradient in the original model of Wheeler et

256 al. (2003) of elastic scanning curves in the $S_r:\ln s^*$ plane is zero i.e. $\kappa_s = 0$). The same
 257 assumption is made here.

258 2.2.2. Retention yield curves

259 Water retention behaviour is described by two yield functions: the wetting retention
 260 yield curve f_{WR} and the drying retention yield curve f_{DR} . Variations of modified suction
 261 occurring inside f_{WR} and f_{DR} result in no changes of S_r (i.e. $dS_r = dS_r^e = 0$). Yielding on
 262 f_{WR} produces plastic increases of S_r (i.e. $dS_r = dS_r^p > 0$), whereas yielding on f_{DR} causes
 263 plastic decreases of S_r (i.e. $dS_r = dS_r^p < 0$). Similarly to the mechanical yield curve, the
 264 expression of the wetting retention yield curve is also normalised:

$$265 \quad f_{WR} = \frac{s_1^* - s}{s_1^*} = 0 \quad (17)$$

266 where s_1^* is the wetting yield stress controlling the occurrence of yielding on f_{WR}
 267 (equivalent to p_0^* for mechanical yielding).

268 The wetting yield stress s_1^* varies with the occurrence of mechanical yielding according
 269 to:

$$270 \quad s_1^* = s_{10}^* \left(\frac{p'_0}{p'_{00}} \right)^{k_2} = s_{10}^* \exp \left(\frac{-k_2}{\lambda - \kappa} \Delta v^p \right) \quad (18)$$

271 where k_2 is a coupling parameter, p'_0 is the mechanical hardening parameter and Δv^p
 272 indicates plastic decreases of specific volume from a reference state. s_{10}^* and p'_{00} are,
 273 respectively, the values of s_1^* and p'_0 at the reference states when $\Delta v^p = 0$.

274 Similarly, the expression of the drying retention yield curve is:

$$275 \quad f_{DR} = \frac{s - s_2^*}{s_2^*} = 0 \quad (19)$$

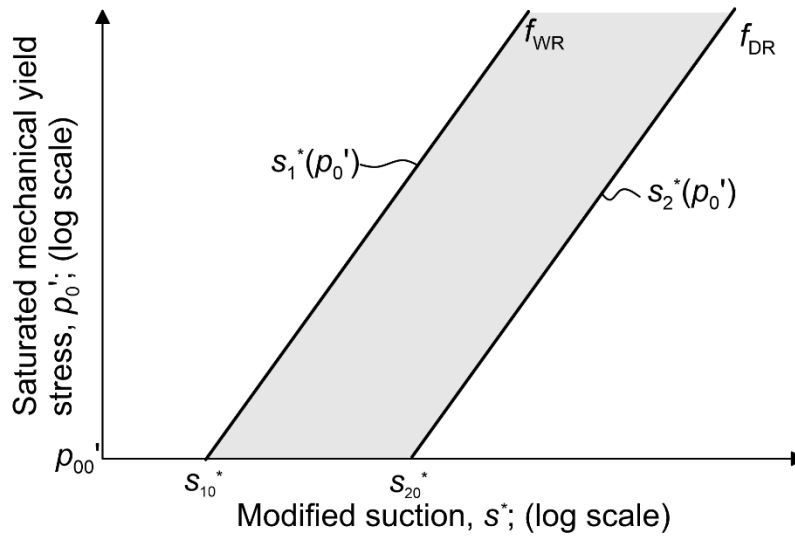
276 where s_2^* is the drying yield stress for f_{DR} which varies with p'_0 (or Δv^p) according to:

$$277 \quad s_2^* = s_{20}^* \left(\frac{p'_0}{p'_{00}} \right)^{k_2} = s_{20}^* \exp \left(\frac{-k_2}{\lambda - \kappa} \Delta v^p \right) \quad (20)$$

278 where s_{20}^* and p'_{00} are, respectively, the values of s_2^* and p'_0 when $\Delta v^p = 0$.

279 Equations 17 and 19 indicate, respectively, that the wetting retention yield curves f_{WR}
 280 and the drying retention yield curve f_{DR} form two parallel straight lines when plotted in
 281 the $\ln s^*:\ln p'_0$ plane (see Figure 3). The positions of these straight lines and their gradient
 282 with respect to $\ln p'_0$ are given by Equations 18 and 20. The current values of the

283 parameters s_{10}^* and s_{20}^* (which correspond, respectively, to the values of s_1^* and s_2^* at
 284 a reference state in which $p'_0 = p'_{00}$) fix the position of f_{WR} and f_{DR} respectively, whereas
 285 the gradient is given by the value of the soil parameter k_2 . Therefore, the parameters
 286 s_{10}^* and s_{20}^* are equivalent to the mechanical hardening parameter p_0' and, hence, can
 287 be viewed as the hardening parameters of the water retention response. Equations 17-
 288 20 are still active under fully saturated conditions, because they track the influence of
 289 mechanical yielding on the potential occurrence of desaturation on drying (i.e. air-entry
 290 point) and re-saturation on wetting or loading (i.e. air-exclusion point).
 291 The spacing between f_{WR} and f_{DR} is assumed constant when plotted in terms of $\ln s^*$ (i.e.
 292 $s_2^* = R \cdot s_1^*$, where R is a soil constant (Lloret-Cabot et al., 2017) and this spacing defines
 293 the current range of values of s^* for which no plastic changes of S_r will occur at a given
 294 value of p'_0 . Hence, the spacing between f_{WR} and f_{DR} in the $\ln s^* : \ln p_0'$ plane defines the
 295 elastic domain of the water retention behaviour (see shaded zone in Figure 3). Yielding
 296 on the drying retention yield curve reduces the values of S_r and causes a coupled
 297 movement of the wetting retention yield curve (Wheeler et al., 2003). Equivalent
 298 comments apply when yielding on f_{WR} .



299

300

Figure 3. Water retention yield curves in $\ln s^* : \ln p_0'$ plane.

301

2.2.3. Hardening law

302

Given that s_{10}^* and s_{20}^* remain constant unless water retention yielding occurs, it is

303

possible to relate them to plastic changes of degree of saturation dS_r^p through the

304

following hardening law:

$$305 \quad \frac{ds_{10}^*}{s_{10}^*} = \frac{ds_{20}^*}{s_{20}^*} = \frac{-dS_r^p}{\lambda_s} \quad (21)$$

306 where λ_s is the gradient of a main wetting/drying curve in the S_r : $\ln s^*$ plane.

307 For completeness, it is useful to include here how the water retention yield stress s_R^*
 308 (where the subscript R is 1 for f_{WR} and 2 for f_{DR}) vary against the water retention and
 309 mechanical hardening parameters:

$$310 \quad \frac{ds_R^*}{s_R^*} = \frac{ds_{R0}^*}{s_{R0}^*} + k_2 \frac{dp'_0}{p'_0} \quad (22)$$

311 Similarly, the mechanical yield stress p_0^* varies with the mechanical and water retention
 312 hardening parameters according to:

$$313 \quad \frac{dp_0^*}{p_0^*} = \frac{dp'_0}{p'_0} + k_1 \frac{ds_{R0}^*}{s_{R0}^*} \quad (23)$$

314 2.2.4. Flow rule

315 Associated flow rules are assumed for the water retention response:

$$316 \quad dS_r^p = dS_r = -d\lambda_R \frac{\partial f_R}{\partial s^*} \quad (24)$$

317 where $d\lambda_R$ is an unknown positive scalar (referred to as the water retention plastic
 318 multiplier) to be found by imposing that the stress point remains on f_R during retention
 319 yielding (consistency condition).

320 Given that $dS_r^e = 0$ (Figure 4), total and plastic variations of S_r are the same ($dS_r = dS_r^p$
 321).

322 2.2.5. Analytical relations for the water retention behaviour

323 The water retention relations just presented result in the following expressions for main
 324 wetting and drying curves:

$$325 \quad S_r = 1 - \lambda_s \ln \left(\frac{s^*}{s_{ex}^*} \right) \quad (25)$$

$$326 \quad S_r = 1 - \lambda_s \ln \left(\frac{s^*}{s_e^*} \right) \quad (26)$$

327 where s_{ex}^* and s_e^* are, respectively, the current air-exclusion and air-entry values of
 328 modified suction (see Figure 4). These air-exclusion and air-entry values of modified

329 suction are related to the saturated preconsolidation stress p'_0 through the saturation and
 330 desaturation lines, respectively (Lloret-Cabot et al., 2017):

$$331 \quad \ln s_{ex}^* = \frac{(\Omega^* - 1)}{\lambda_s^*} + k_2 \ln p'_0 \quad (27)$$

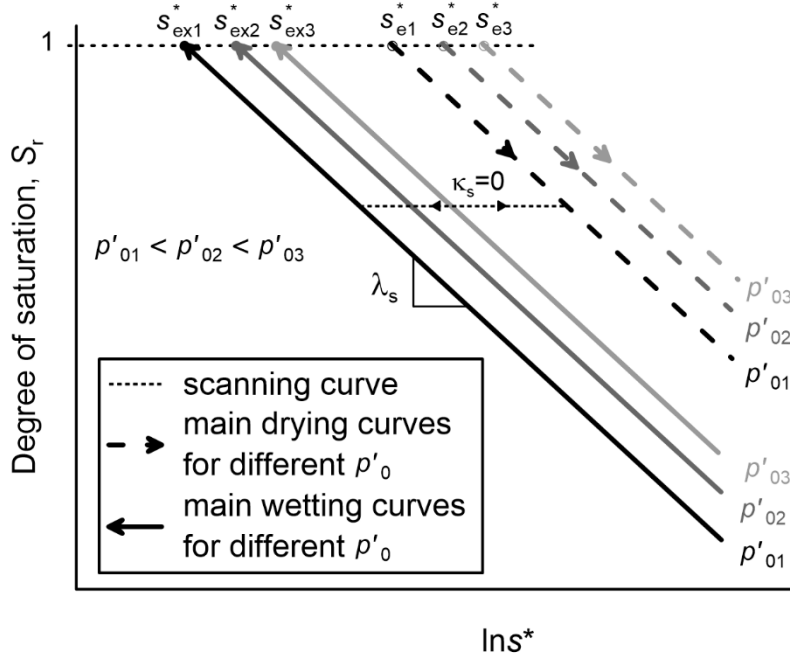
$$332 \quad \ln s_e^* = \frac{(\Omega^* - 1)}{\lambda_s^*} + k_2 \ln p'_0 + \ln R \quad (28)$$

333 where λ_s^* and Ω^* are soil constants corresponding to the gradient and intercept,
 334 respectively, of the unsaturated normal compression planar surface for S_r derived in
 335 Lloret-Cabot et al. (2017). λ_s^* can be expressed in terms of soil constants λ_s , k_1 and k_2
 336 and Ω^* can be expressed in terms of soil constants N , N^* , λ , κ , λ_s and k_1 (see Appendix
 337 A), where N^* is the intercept of the unsaturated normal compression planar surface for
 338 v derived in Lloret-Cabot et al. (2017).

339 Combining main wetting and main drying equations with the saturation and
 340 desaturation lines, respectively, the expressions of the main wetting and main drying
 341 curves can be expressed in terms of p'_0 :

$$342 \quad S_r = 1 + \left[(\Omega^* - 1)(1 - k_1 k_2) + k_2 \lambda_s \ln p'_0 \right] - \lambda_s \ln s^* \quad (29)$$

$$343 \quad S_r = 1 + \left[\lambda_s \ln R + (\Omega^* - 1)(1 - k_1 k_2) + k_2 \lambda_s \ln p'_0 \right] - \lambda_s \ln s^* \quad (30)$$



344 $\ln s^*$
 345 Figure 4. Main wetting and main drying water retention curves for constant values of
 346 p'_0 in the S_r : $\ln s^*$ plane.

347 2.3. Model responses

348 There are six possible responses in the GCM to represent mechanical and water
349 retention behaviour of soils under saturated and unsaturated conditions. Each of them
350 is identified hereafter by an integer number assigned to the variable “STRPTH”:

- 351 (1) STRPTH=1 is for purely elastic behaviour ($\Delta\epsilon^p = \mathbf{0}$ and $\Delta S_r = 0$).
352 (2) STRPTH=2 is for yielding on only f_{WR} ($\Delta\epsilon^p = \mathbf{0}$ and $\Delta S_r > 0$).
353 (3) STRPTH=3 is for yielding on only f_{DR} ($\Delta\epsilon^p = \mathbf{0}$ and $\Delta S_r < 0$).
354 (4) STRPTH=4 is for yielding on only f_M ($\Delta\epsilon^p \neq \mathbf{0}$ and $\Delta S_r = 0$).
355 (5) STRPTH=5 is for simultaneous yielding on f_M and f_{WR} ($\Delta\epsilon^p \neq \mathbf{0}$ and $\Delta S_r > 0$).
356 (6) STRPTH=6 for simultaneous yielding on f_M and f_{DR} ($\Delta\epsilon^p \neq \mathbf{0}$ and $\Delta S_r < 0$).

357 Transitions from unsaturated to saturated conditions (saturation) occur whilst on f_{WR} .
358 This means that an initially unsaturated soil ($S_r < 1$) can only saturate during stress paths
359 that involve yielding on f_{WR} (i.e. STRPTH=2 or STRPTH=5). Once the soil is saturated,
360 further increases of S_r are prevented (i.e. flow rule no longer applies on f_{WR}) and the
361 consistency condition on f_{WR} is removed so that the stress point can pass beyond f_{WR}
362 (see Lloret-Cabot et al., 2017, Lloret-Cabot et al., 2018ab for details). Transitions in the
363 reverse direction (desaturation), occur whilst on f_{DR} . In this case, an initially saturated
364 soil ($S_r = 1$) can only desaturate during stress paths that involve yielding on f_{DR} (i.e.
365 STRPTH=3 or STRPTH=6).

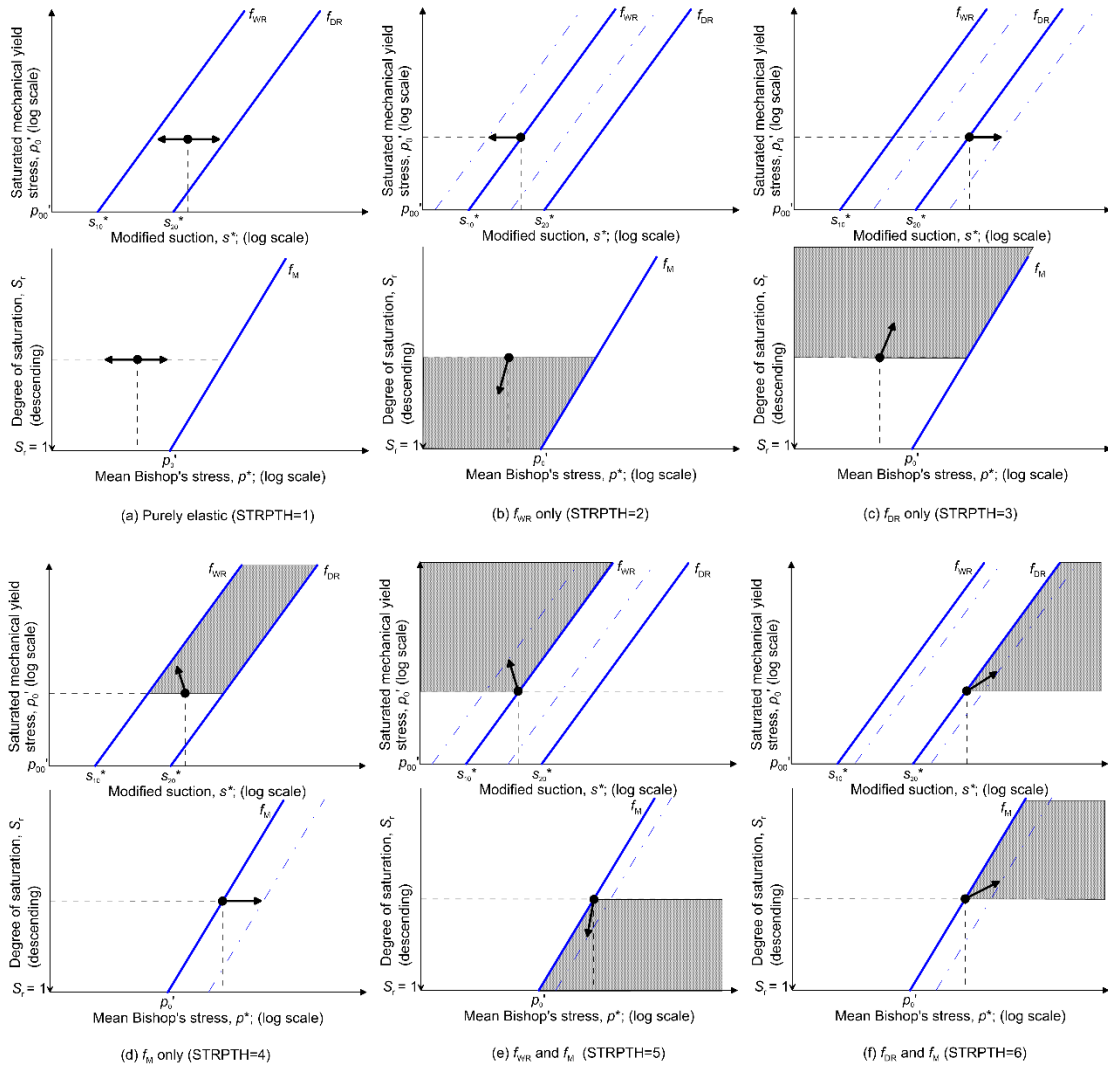
366 Typical examples of the six possible responses in the GCM are illustrated in Figure 5
367 for unsaturated states. Each response is represented by a pair of plots. The top plot
368 shows the water retention behaviour in the $\ln p_0' : \ln s^*$ plane and the bottom one, the
369 mechanical response in the $S_r : \ln p^*$ plane. The initial position of each yield curve is
370 indicated by a solid line whereas, if yielding occurs, the corresponding final positions
371 of the yield curves are indicated by chain-dotted lines. Arrows indicate the movement
372 of the stress point and the shaded zone indicates other possible positions of the final
373 stress point that would also activate the same type of model response. For clarity, the
374 responses are shown for isotropic stress conditions, but equivalent conclusions apply in
375 general stress space.

376 Figure 5a shows an example of purely elastic behaviour (STRPTH=1) and corresponds
377 to a situation where the final stress point remains inside the elastic domain (i.e. $f_{WR} \leq$
378 $FTOL$ & $f_{DR} \leq FTOL$ & $f_M \leq FTOL$, where $FTOL$ is a specified tolerance) so that all

379 yield curves remain at the same initial position. In contrast, Figures 5b and 5c show
380 typical responses for retention yielding alone (STRPTH=2 or 3) causing plastic changes
381 of S_r . Note that in each of these two cases the retention curve not being yielded has also
382 moved from its initial position as a consequence of the associated movement defined
383 by Equation 21. No plastic straining occurs when STRPTH=2 or 3 because the stress
384 path remains inside f_M (Figures 5b and 5c). As a consequence, the saturated mechanical
385 yield stress p_0' remains unchanged (and, hence, the mechanical yield curve does not
386 move).

387 Figure 5d shows an example of yielding on only f_M (STRPTH=4) where only the
388 mechanical yield curve moves from its initial position as a consequence of plastic
389 straining. Examples of yielding on two yield curves simultaneously are illustrated in
390 Figures 5e and 5f. In these, plastic straining and plastic changes of S_r occur at the same
391 time and, as a result, all yield curves move.

392 The forms of Equation 8 (for the mechanical response) and Equations 18 and 20 (for
393 water retention response) plotted in Figure 5 demonstrate one of the computational
394 advantages of the reformulated equations of the GCM discussed earlier. Equation 8, for
395 example, corresponds to the integrated form of how the coupling of the water retention
396 behaviour on the mechanical response is represented within the GCM. Similarly,
397 Equations 18 and 20, correspond to the integrated form of the coupling of the
398 mechanical response on the water retention. As further demonstrated later, these
399 integrated forms of the couplings between mechanical and retention responses facilitate
400 the identification of the active model response and simplify the intersection problem
401 arising when a stress path crosses a yield curve of the model.



402

403

404

Figure 5 Typical model responses for isotropic stress states under unsaturated conditions.

405

3. MECHANICAL AND WATER RETENTION RELATIONS

406

407

408

409

410

411

412

413

414

415

When using the finite element method in problems involving saturated soils that may eventually desaturate, the *local* (i.e. within the element) integration of the coupled constitutive model representing the material behaviour of the soil involves the solution of both the mechanical and water retention incremental relations. During a typical finite element iteration in such problems, the nodal displacement and pore fluid pressures (including water and air) increments are usually found from the solution of the discretized *global* system of equations, typically involving equilibrium and mass balance relations (e.g. Olivella et al., 1996). Nodal displacement increments are combined with the strain-displacement relations to find the corresponding strain increments at a finite number of Gauss points within each element and, similarly, nodal

416 pore fluid pressures increments are combined to find the corresponding increment of
 417 suction at each Gauss point. The known strain and suction increments can be then used
 418 at the local level to find the corresponding increments of stresses and degree of
 419 saturation via integration of the coupled constitutive model. It is hence convenient in
 420 finite element analysis (FEA) to express the local integration algorithm in terms of the
 421 *known* strain and suction increments (i.e. strain-driven algorithm). Because of their
 422 compatibility in FEA, this section focuses on strain-driven formulations to integrate the
 423 constitutive relations of the GCM, extending to unsaturated conditions the work on
 424 explicit substepping algorithms with automatic error control proposed in Sloan et al.
 425 (2001) for saturated soils.

426 3.1. Formulation of the problem

427 The numerical integration of a constitutive model for unsaturated soils involves the
 428 solution of an initial value problem (IVP) defined by the incremental relationships of
 429 the model, the initial (or current) state, the corresponding parameters of the model and,
 430 in the context of strain-driven formulations, a given pair of $\Delta\boldsymbol{\varepsilon}$ and Δs (Δ denotes a finite
 431 variation). Expressing the relations of the GCM by means of a strain-driven formulation
 432 is very convenient because, irrespective of the model response active, Δs^* can be
 433 computed correctly from the initial (or current) state at i and the exact updates of
 434 specific volume v and matric suction s at $i+1$:

$$435 \quad {}^{i+1}s = {}^i s + \Delta s \quad (31)$$

$$436 \quad {}^{i+1}v = {}^i v \exp(-\Delta\varepsilon_v) \quad (32)$$

437 The correct update of s^* at $i+1$ is then given by:

$$438 \quad {}^{i+1}s^* = {}^{i+1}s \frac{{}^{i+1}v - 1}{{}^i v} \quad (33)$$

439 From where the correct increment of modified suction can be calculated:

$$440 \quad \Delta s^* = {}^{i+1}s^* - {}^i s^* \quad (34)$$

441 Once the increments of modified suction are known, the remaining incremental
 442 quantities can be expressed in a general IVP form as follows. The first two equations
 443 describe the mechanical response (Bishop's stress – strain relations) and the second pair
 444 the water retention response (modified suction – degree of saturation relations):

$$445 \quad \Delta \boldsymbol{\sigma}^* = \mathbf{D}_e \Delta \boldsymbol{\varepsilon} - \Delta \lambda_M \mathbf{D}_e \mathbf{a}_M \quad (35)$$

446 $\Delta p_0' = \Delta \lambda_M B_M$ (36)

447 $\Delta S_r = -\Delta \lambda_R a_R$ (37)

448 $\Delta s_{R0}^* = -\Delta \lambda_R B_R$ (38)

449 where the subscript M indicates mechanical response and the subscript R indicates
 450 retention response (with 1 for f_{WR} and 2 for f_{DR}), $\Delta \lambda_M$ and $\Delta \lambda_R$ are the respective plastic
 451 multipliers, p_0' and s_{R0}^* are the respective hardening parameters, \mathbf{a}_M is the gradient of
 452 the mechanical yield curve with respect to Bishop's stress, a_R is the derivative of the
 453 retention yield curve with respect to modified suction, B_M is a scalar function for the
 454 mechanical response and B_R is a scalar function for the retention response.

455 *3.1.1. Elastic behaviour*

456 Elastic behaviour under saturated or unsaturated conditions (STRPTH=1) is a particular
 457 case of the general problem defined by Equations 35-38, noting that for STRPTH=1,
 458 the mechanical and retention plastic multipliers are both zero.

459 Elastic behaviour is represented in the GCM in terms of the secant bulk \bar{K} and shear
 460 \bar{G} moduli, equivalent to saturated soils (Sheng et al., 2000). This representation ensures
 461 the correct computation of Bishop's stresses at the intersection of the stress path with
 462 one of the three yield curves of the model, when the computed response passes from
 463 elastic to plastic. Integrating Equation 4 for p^* and ε_v^e the following analytical
 464 expression for \bar{K} can be found (Lloret-Cabot et al., 2016):

465
$$\bar{K} = \frac{i p^*}{\Delta \varepsilon_v^e} \left[\exp \left(\frac{i v (1 - \exp(-\Delta \varepsilon_v^e))}{\kappa} \right) - 1 \right] \quad (39)$$

466 where $i p^*$ and $i v$ are, respectively, the mean Bishop's stress and specific volume at the
 467 start of the volumetric strain increment i . A corresponding appropriate expression for
 468 \bar{G} should also be used (the form of this will depend upon what assumption is made for
 469 the tangent shear modulus G , see Potts and Zdravkovic, 1999).

470 *3.1.2. Elasto-plastic behaviour*

471 Equations 35-38 are valid for all types of elasto-plastic yielding, including unsaturated
 472 and saturated conditions, noting that, under saturated conditions, increases of S_r are
 473 prevented.

474 Some useful simplifications are possible for the particular cases of yielding on one
 475 water retention curve alone (STRPTH=2 or 3). Due to the absence of mechanical
 476 yielding, p_0' remains unchanged which means that the mechanical plastic multiplier is
 477 zero and then the increment of Bishop's stress can be computed exactly, using the
 478 approach discussed for the elastic case. Also, given that $\Delta\lambda_M = 0$, it is possible to
 479 compute exact values of degree of saturation at the updated exact value of modified
 480 suction (Equation 33) using Equation 25 for yielding on only f_{WR} or Equation 26 for
 481 yielding on only f_{DR} .

482 For mechanical yielding alone (STRPTH=4), whether the soil is saturated or
 483 unsaturated, $\Delta\lambda_R = 0$ because $\Delta S_r = 0$. This means that the expression for $\Delta\lambda_M$ can be
 484 found in the same way as that of the plastic multiplier for the MCC (see Sloan et al.,
 485 (2001) for details).

486 Hence, the only two mechanisms that require the derivation of a new expression for the
 487 mechanical and water retention plastic multipliers correspond to simultaneous yielding
 488 on f_M and f_R (STRPTH=5 or 6). When f_M and f_R yield simultaneously, it is necessary to
 489 impose the consistency condition on both to find expressions for $\Delta\lambda_M$ and $\Delta\lambda_R$ in terms
 490 of $\Delta\boldsymbol{\varepsilon}$ and Δs :

$$491 \quad df_M = 0 \Rightarrow \left(\frac{\partial f_M}{\partial \boldsymbol{\sigma}^*} \right)^T \mathbf{D}_e (\Delta\boldsymbol{\varepsilon} - \Delta\boldsymbol{\varepsilon}^p) + \frac{\partial f_M}{\partial p_0^*} \left[\frac{\partial p_0^*}{\partial p_0'} \Delta p_0' + \frac{\partial p_0^*}{\partial S_r} \Delta S_r \right] = 0 \quad (40)$$

$$492 \quad df_R = 0 \Rightarrow \left(\frac{\partial f_R}{\partial s^*} \right) \Delta s^* + \frac{\partial f_R}{\partial s_R^*} \left[\frac{\partial s_R^*}{\partial s_{R0}^*} \Delta s_{R0}^* + \frac{\partial s_R^*}{\partial p_0'} \Delta p_0' \right] = 0 \quad (41)$$

493 General expressions for the mechanical and retention plastic multipliers can be found
 494 by solving simultaneously the above expressions, after inserting the relevant hardening
 495 laws (Equations 9 and 21) and the relevant flow rules (Equations 10 and 24):

$$496 \quad \Delta\lambda_M = \frac{\mathbf{D}_M \Delta\boldsymbol{\varepsilon} + C_M \Delta s^*}{A + \mathbf{D}_M \mathbf{a}_M} \quad (42)$$

$$497 \quad \Delta\lambda_R = \frac{D_R \Delta s^* + C_R \Delta\boldsymbol{\varepsilon}}{A + \mathbf{D}_M \mathbf{a}_M} \quad (43)$$

498 where \mathbf{D}_M , D_R , C_M , C_R and A are given by:

$$499 \quad \mathbf{D}_M = \mathbf{a}_M^T \mathbf{D}_e \quad (44)$$

$$500 \quad D_{\mathbf{R}} = \frac{-1}{B_{\mathbf{R}}} \left(\mathbf{D}_{\mathbf{M}} \mathbf{a}_{\mathbf{M}} - \frac{\partial f_{\mathbf{M}}}{\partial p_0^*} \frac{\partial p_0^*}{\partial p_0'} B_{\mathbf{M}} \right) \frac{\partial s_{\mathbf{R}0}^*}{\partial s_{\mathbf{R}}^*} \quad (45)$$

$$501 \quad C_{\mathbf{M}} = \frac{1}{B_{\mathbf{R}}} \frac{\partial f_{\mathbf{M}}}{\partial p_0^*} \frac{\partial p_0^*}{\partial S_r} \frac{\partial s_{\mathbf{R}0}^*}{\partial s_{\mathbf{R}}^*} \frac{\partial f_{\mathbf{R}}}{\partial s^*} \quad (46)$$

$$502 \quad \mathbf{C}_{\mathbf{R}} = \frac{B_{\mathbf{M}}}{B_{\mathbf{R}}} \begin{bmatrix} \frac{\partial s_{\mathbf{R}0}^*}{\partial s_{\mathbf{R}}^*} & \frac{\partial s_{\mathbf{R}}^*}{\partial p_0'} \end{bmatrix} \mathbf{D}_{\mathbf{M}} \quad (47)$$

$$503 \quad A = -(1 - k_1 k_2) \frac{\partial f_{\mathbf{M}}}{\partial p_0^*} \frac{\partial p_0^*}{\partial p_0'} B_{\mathbf{M}} \quad (48)$$

504 The expressions for the scalar functions $B_{\mathbf{M}}$ and $B_{\mathbf{R}}$ are:

$$505 \quad B_{\mathbf{M}} = \frac{\partial p_0'}{\partial \varepsilon_v^p} \frac{\partial f_{\mathbf{M}}}{\partial p^*} \quad (49)$$

$$506 \quad B_{\mathbf{R}} = \frac{\partial s_{\mathbf{R}0}^*}{\partial S_r^p} \frac{\partial f_{\mathbf{R}}}{\partial s^*} \quad (50)$$

507 As noted earlier, Δs^* can be computed exactly when $\Delta \varepsilon$ and Δs are known (Equation
508 34).

509 3.2. Algorithm for the identification of the model response

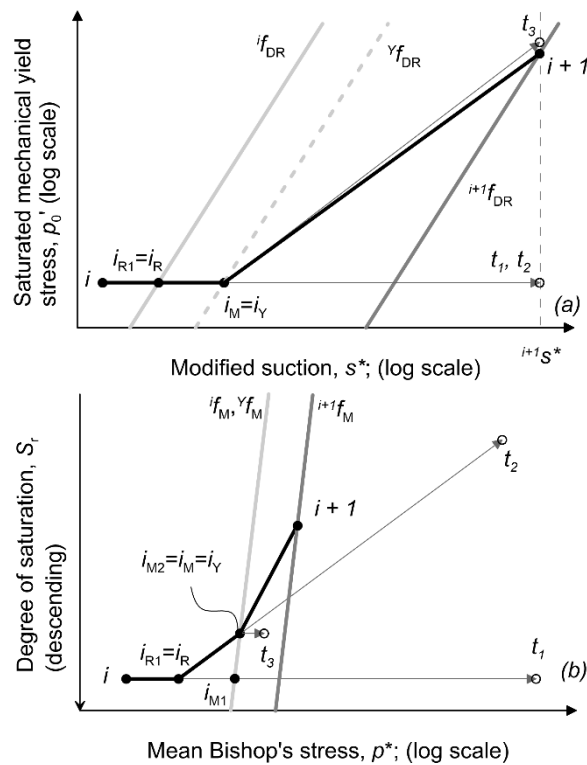
510 The reformulation of GCM has facilitated the development of an algorithm that
511 identifies, unambiguously, which is the model response activated by the given
512 increments $\Delta \varepsilon$ and Δs . Once the model response is known, all variables are updated
513 using the appropriate set of incremental relations derived in the previous section. In
514 such update, the algorithm automatically checks if the stress path intersects a yield
515 curve and, if so, finds the corresponding intersection by using the Pegasus algorithm
516 proposed by Dowell and Jarratt (1972), and widely tested for saturated soil models
517 (Sloan et al., 2001, Abbo, 1997, Sheng et al., 2000, Pedroso et al., 2008, Zhao et al.,
518 2005).

519 Figure 6 illustrates the various steps carried out by the algorithm to decide how to
520 integrate the given increments of $\Delta \varepsilon$ and Δs correctly. The case illustrated corresponds
521 to the most challenging scenario in which, from an initial point inside the elastic
522 domain, the known increments $\Delta \varepsilon$ and Δs end up activating yielding on two yield
523 curves. The particular model response plotted corresponds to STRPTH=6, but
524 equivalent results are obtained for STRPTH=5. A maximum of three different trials is

525 needed to handle correctly this problem. This means that, in the worst situation, the
 526 algorithm needs to break $\Delta\epsilon$ and Δs in three parts. All other cases (i.e. initial stress point
 527 on one or two yield curves) are a simplified version of this one and, hence, follow the
 528 same logic.

529 Figure 6 is in two parts. Part a shows the full sequence of steps in the $\ln p_0' : \ln s^*$ plane
 530 whereas Part b illustrates their counterparts in the $S_r : \ln p^*$ plane (note that the values of
 531 S_r in the vertical axis increase downwards). The current stress point is indicated by i
 532 and is assumed to be inside the three yield curves of the model (note that $i f_{WR}$ is not
 533 included in Figure 6a for clarity, but its location is to the left of point i , see Figure 5 for
 534 reference). *Trial 1* (indicated by t_1) is purely elastic ($\Delta S_r = 0$ and $\Delta p_0' = 0$) and ends up
 535 outside both $i f_{DR}$ (see Figure 6a) and $i f_M$ (see Figure 6b). Hence, it is necessary to check
 536 which of these two yield curves is hit first by *trial 1*. This problem involves finding two
 537 scalars (α_1 for f_{DR} and α_2 for f_M), both between 0 and 1, that indicate the portion of $\Delta\epsilon$
 538 and Δs required to move, elastically, the stress point i to the corresponding intersection
 539 point (indicated as i_{R1} for f_{DR} and i_{M1} for f_M). The lower value of the two scalars
 540 corresponds to the yield curve hit first by *trial 1*. In the example represented in Figure
 541 6, f_{DR} is the yield curve hit first (i.e. $\alpha_1 < \alpha_2$). Hence, a purely elastic update of the stress
 542 point from i to the intersection point i_{R1} is then carried out using the appropriate portion
 543 of the given increments (i.e. $\alpha_1 \Delta\epsilon$ and $\alpha_1 \Delta s$). The next step is to compute *Trial 2*
 544 (indicated as t_2) starting from i_{R1} (also indicated as i_R in Figure 6) and now assuming
 545 yielding on only f_{DR} . Importantly, *Trial 2* uses only the not yet integrated part of the
 546 increments of strains and suction i.e. $(1-\alpha_1)\Delta\epsilon$ and $(1-\alpha_1)\Delta s$. Given that yielding on only
 547 f_{DR} is the model response assumed in computing t_2 , the mechanical hardening parameter
 548 p_0' is constant (see Figure 6a) and the corresponding value of S_r is exact because it can
 549 be calculated inserting the exact value of modified suction at t_2 (which equals that
 550 calculated in t_1 , see Figure 6a) in the equation of the main drying curve (Equation 26).
 551 A second intersection problem arises, now with $i f_M$ (Figure 6). This second intersection
 552 problem involves finding a scalar β (also between 0 and 1) that defines the portion of
 553 $(1-\alpha_1)\Delta\epsilon$ and $(1-\alpha_1)\Delta s$ required to move, under yielding on only f_{DR} , the stress point
 554 from i_R to i_M (also indicated as i_Y in Figure 6 to highlight that the stress point lies on
 555 both yield curves). Once β has been found, the stress point is updated from i_R to i_M
 556 assuming yielding on only f_{DR} and using the relevant portion of strain and suction
 557 increments i.e. $\beta(1-\alpha_1)\Delta\epsilon$ and $\beta(1-\alpha_1)\Delta s$. In moving the stress point from i_R to i_M ,
 558 yielding on only f_{DR} is occurring and, consequently, $i f_{DR}$ yields to $Y f_{DR}$ as indicated by

559 the thicker light dashed line in Figure 6a. At this stage, the stress point is on both yield
 560 curves. A final *trial 3*, now assuming yielding on only f_M , needs to be computed to
 561 determine whether the portion not yet integrated of strains and suction increments (i.e.
 562 $(1-\beta)(1-\alpha_1)\Delta\varepsilon$ and $(1-\beta)(1-\alpha_1)\Delta s$) activates yielding on only f_M or simultaneous yielding
 563 on f_M and f_{DR} . Conveniently, the algorithm *knows* at this point that yielding on only f_{DR}
 564 is not possible because *trial 2* fell outside f_M when assuming yielding on only f_{DR} . In
 565 the example of Figure 6, *trial 3* ends up outside f_{DR} meaning that this final portion of
 566 $\Delta\varepsilon$ and Δs , moving the stress point from i_Y to $i+1$, has to be integrated assuming
 567 simultaneous yielding on f_M and f_{DR} . The stress path followed to integrate the full size
 568 of $\Delta\varepsilon$ and Δs is indicated in the figure by a thick black solid line and the final positions
 569 of f_M and f_{DR} at $i+1$ are indicated by a lighter thick solid line.
 570



571
 572 Figure 6 Example of a typical integration of the GCM starting from inside the three
 573 yield curves and ending up activating yielding on two yield surfaces (STRPTH=6).
 574
 575 A more formalised description of the sequence of steps followed by the algorithm to
 576 determine which is the active response of the GCM is presented in Appendix B.

577 3.3. Yield intersections

578 The given increments of $\Delta\varepsilon$ and Δs may change the stress state from elastic to elasto-
579 plastic within the increment. In the context of the GCM, this means that a *trial* intersects
580 at least one yield curve. Note that during a transition from unsaturated to saturated
581 conditions, there might also be the reverse situation (i.e. from elasto-plastic to elastic
582 within an individual increment) in wetting paths that saturate during collapse
583 compression (Lloret-Cabot et al., 2017, Lloret-Cabot et al., 2018) i.e. it is possible to
584 have within a single increment a first part (while unsaturated) that is elasto-plastic and
585 a second part (while saturated) that is elastic. The intersection point in such cases is
586 controlled by the value of S_r but it is found in an equivalent way to any other intersection
587 problem. All of these intersections are found here using the Pegasus algorithm proposed
588 by Dowell and Jarratt (1972) and extensively used in the literature (e.g. Sloan et al.,
589 2001, Abbo, 1997, Sheng et al., 2000, Pedroso et al., 2008, Zhao et al., 2005). Its
590 algorithmic form is summarised in Appendix C for completeness).

591 There might situations in which the given increments of strain and suction intersect a
592 yield surface twice, even though initial and final stress states are both inside the yield
593 locus. Such situation is aggravated when using too large increments and, hence, the use
594 of sufficiently small increments of strain and suction is recommended. Sołowski &
595 Sloan (2012) discuss this intersection problem further in the context of the BBM
596 (Alonso et al. 1990).

597 Another possible intersection problem is that referred to as “elasto-plastic unloading”
598 (Sloan et al. 2001). The solution to this problem in the context of the GCM is equivalent
599 to that proposed for critical state saturated models (e.g. Sloan et al., 2001, Abbo, 1997,
600 Sheng et al., 2000, Pedroso et al., 2008).

601 3.4. Drift correction

602 Similarly to what is observed in explicit integration schemes for saturated soils, in
603 unsaturated soils too the stress point at the end of each integration step/substep may
604 *drift* from the yield condition, so that $|f_A| > FTOL$. The extent of this drift primarily
605 depends on the accuracy of the integration scheme used and, in general, when using
606 substepping strategies with error control, drift correction is rarely needed Sołowski et
607 al. (2012). However, as advised in Sloan et al. (2001), it is prudent to consider the
608 possibility to correct a potential drift at the end of each integrated step/substep.

609 In the context of the GCM, a correction of the drift of the stress point is only potentially
 610 needed when mechanical yielding occurs, whether this implies yielding on only f_M
 611 (STRPTH=4) or simultaneous yielding on f_M and a retention yield curve (STRPTH=5
 612 or 6). Yielding on a retention yield curve alone (STRPTH=2 or 3) does not require any
 613 drift correction in the context of strain-driven formulations because, as explained
 614 earlier, an exact update of all relevant variables is possible.

615 The strategy to correct the stress point in the GCM adopts the drift correction method
 616 recommended in Potts and Gens (1984) for saturated soils. The extension of such
 617 strategy to unsaturated soils includes the assumption that, in addition to imposing no
 618 strain variations i.e. $\delta\boldsymbol{\varepsilon} = \mathbf{0}$ during the correction of the stress point, also suction remains
 619 unchanged i.e. $\delta s = 0$. The latter assumption has been successfully used for the
 620 numerical integration of many other unsaturated soil models (e.g. Sánchez et al. 2008,
 621 Sołowski and Gallipoli 2010ab).

622 Assuming $\delta\boldsymbol{\varepsilon} = \mathbf{0}$ and $\delta s = 0$ means that the correction of modified suction δs^* and
 623 specific volume δv are both zero. Given that $\delta s^* = 0$, the correction of degree of
 624 saturation δS_r and of the water retention hardening parameters δs_{R0}^* are all also zero.
 625 The correction of Bishop's stresses $\delta\boldsymbol{\sigma}^*$ and mechanical hardening parameter $\delta p_0'$ are
 626 unknown quantities and can be found by expanding f_M in Taylor series about the stress
 627 point to be corrected i . Neglecting second order terms and above, this can be expressed
 628 by:

$$629 \quad f_M \approx {}^i f_M + \left(\frac{\partial f_M}{\partial \boldsymbol{\sigma}^*} \right) \delta \boldsymbol{\sigma}^* + \left(\frac{\partial f_M}{\partial p_0'} \right) \left(\frac{\partial p_0'}{\partial p_0^*} \delta p_0^* + \frac{\partial p_0'}{\partial S_r} \delta S_r \right) \quad (51)$$

630 where $\delta S_r = 0$.

631 Equations 35 and 36 mean that for the total strain increment to remain zero, the
 632 corrections in the Bishop's stress and mechanical hardening parameter are,
 633 respectively:

$$634 \quad \delta \boldsymbol{\sigma}^* = -\delta \lambda_M \mathbf{D}_e \mathbf{a}_M \quad (52)$$

$$635 \quad \delta p_0' = \delta \lambda_M B_M \quad (53)$$

636 where $\delta \lambda_M$ is an unknown multiplier and \mathbf{D}_e , \mathbf{a}_M and B_M are all evaluated at i .

637 The following expression for $\delta \lambda_M$ is found by combining Equations 51-53, after
 638 imposing that $f_M = 0$:

$$639 \quad \delta\lambda_M = \frac{f_M}{\mathbf{a}_M^T \mathbf{D}_e \mathbf{a}_M - \frac{\partial f_M}{\partial p_0^*} \frac{\partial p_0^*}{\partial p_0'} B_M} \quad (54)$$

640 While there is no need to correct s^* , s_{R0}^* , S_r nor v , a correction needs to be applied to
 641 the mechanical and the water retention yield stresses:

$$642 \quad \delta p_0^* = \frac{p_0^*}{p_0'} \delta\lambda_M B_M \quad (55)$$

$$643 \quad \delta s_R^* = k_2 \frac{s_R^*}{p_0'} \delta\lambda_M B_M \quad (56)$$

644 where all variables are evaluated at i .

645 4. EXPLICIT SUBSTEPPING INTEGRATION SCHEMES

646 This section presents two explicit substepping integration schemes for the numerical
 647 integration of the GCM. The first one corresponds to the second order accurate
 648 modified Euler with substepping (ME2) whereas the second one is the fifth order
 649 accurate Runge-Kutta-Dormand-Prince (RKDP5) with substepping. The notation
 650 adopted extends that employed by Sloan et al. (2001) to unsaturated soils, making
 651 explicit the dependence of the initial value problem (IVP) on the specific volume (as in
 652 critical state models for saturated soils, see Lloret-Cabot et al., 2016) and also on the
 653 degree of saturation. A comparative analysis of the relative numerical performance of
 654 these two substepping integration schemes is provided in the next section.

655 For the same reasons given in the drift correction approach, the application of a
 656 substepping strategy with error control in the GCM is unnecessary in absence of
 657 mechanical yielding, whether this means elastic behaviour or yielding on only one
 658 retention curve (i.e. STRPTH=1, 2 or 3). In contrast, a substepping strategy with error
 659 control becomes extremely convenient for the numerical integration of the incremental
 660 relations of the GCM when mechanical yielding is active, because for STRPTH=4, 5
 661 or 6 the incremental constitutive laws are not integrable analytically. In such cases, the
 662 key to ensure an accurate and efficient numerical integration is to control the local error
 663 in the computed variables arising due to the inexact integration of the integration
 664 scheme. In a substepping integration scheme, this local error is controlled by using a
 665 measure of the truncation error, which is estimated as the difference between the
 666 approximate solutions from two integration schemes of different order (Shampine,

667 1994). How much these two approximations differ from each other is indicative of the
 668 deviation of the numerical solution from the true solution and, hence, this difference
 669 can be used to estimate the truncation error and to automatically adjust, then, the size
 670 of the current integration step/substep.

671 To extend to unsaturated conditions the formulation of Sloan et al. (2001) presented for
 672 saturated soils, it is useful to express the equations involved in the problem in terms of
 673 a pseudo-time T :

$$674 \quad T = \frac{t - {}^{i=0}t}{\Delta t} \quad (57)$$

675 where $t = {}^{i=0}t$ is the time at the start of the strain increment $\Delta\boldsymbol{\varepsilon}$ and suction increment Δs
 676 (i.e. $T = 0$), $t = {}^0t + \Delta t$ is the time at the end of the strain and suction increments (i.e. T
 677 $= 1$) and $0 \leq T \leq 1$.

$$678 \quad \frac{ds}{dT} \cong \Delta s \quad (58)$$

$$679 \quad \frac{dv}{dT} \cong v \exp(-\Delta\varepsilon_v) \quad (59)$$

$$680 \quad \frac{ds^*}{dT} \cong \Delta s^* \quad (60)$$

$$681 \quad \frac{d\boldsymbol{\sigma}^*}{dT} \cong \Delta\boldsymbol{\sigma}^* = \mathbf{D}_e\Delta\boldsymbol{\varepsilon} - \Delta\lambda_M\mathbf{D}_e\mathbf{a}_M \quad (61)$$

$$682 \quad \frac{dp_0'}{dT} \cong \Delta p_0' = \Delta\lambda_M B_M \quad (62)$$

$$683 \quad \frac{dS_r}{dT} \cong \Delta S_r = -\Delta\lambda_R a_R \quad (63)$$

$$684 \quad \frac{ds_{R0}^*}{dT} \cong \Delta s_{R0}^* = \Delta\lambda_R B_R \quad (64)$$

685 where the subscript “R” is 1 for f_{WR} and 2 for f_{DR} .

686 The system of Equations 58-64 defines an initial value problem (IVP) that can be
 687 integrated over T knowing the values at the initial (or current) state i of modified suction
 688 ${}^i s^*$, Bishop’s stress ${}^i \boldsymbol{\sigma}^*$, hardening parameters ${}^i p_0'$ and ${}^i s_{R0}^*$, specific volume ${}^i v$ and degree
 689 of saturation ${}^i S_r$, together with the imposed $\Delta\boldsymbol{\varepsilon}$ and Δs . Similarly to the strain-driven
 690 numerical integration of the MCC for $\Delta\boldsymbol{\varepsilon}$, also Δs is fixed in the strain-driven integration
 691 of the GCM presented here, meaning that the IVP is solved assuming constant strain
 692 and suction rates, $\Delta\boldsymbol{\varepsilon}/\Delta t$ and $\Delta s/\Delta t$, during each step/substep.

693 The form of the system of equations 59-64 is a direct consequence of assuming that not
694 only the mechanical behaviour of unsaturated soils can be represented as an elasto-
695 plastic process but also the water retention response (Wheeler et al. 2003). Under these
696 considerations, the system of equations 59 to 64 encompasses saturated and unsaturated
697 conditions and incorporates the coupling between the mechanical and the water
698 retention behaviour. Although the specific GCM equations are used, the same
699 integration scheme is applicable to any model that, in addition to assuming elasto-
700 plastic formulations for the mechanical and the water retention responses, accounts for
701 the coupling between mechanical and water retention behaviour via plastic volumetric
702 strains and plastic changes of degree of saturation.

703 A substepping integration scheme integrates the incremental relations of a constitutive
704 model by automatically adjusting the size of the given integration interval (or
705 increment) depending on a relative measure of the local error, *REL*. When *REL* is
706 larger/smaller than a specified tolerance (i.e. *STOL*), the current size of the integration
707 step/substep is reduced/increased according to $\Delta T^{i+1} = r^i \Delta T$ where the scalar *r* is
708 estimated as follows. Based on the assumption that the size of a step/substep varies
709 proportionally to a measure of the local error *r*, Sloan et al. (2001) suggest to use $r \cong$
710 $0.9(STOL/REL_n)^{1/2}$ for the second order accurate modified Euler with substepping and
711 $r \cong 0.9(STOL/REL_n)^{1/5}$ for the fifth order accurate Runge-Kutta-Dormand-Prince with
712 substepping. An additional constraint for the scalar *r* is to bound its values between 0.1
713 and 1.1 to limit the change in size during two consecutive substeps, and a maximum
714 number of substeps needs to be also specified (see Sloan et al. (2001) for full details).

715 A major point of the substepping integration schemes presented here is that the measure
716 of the relative error *REL* is estimated for σ^* , p_0' , S_r and S_{R0}^* . The reason for treating
717 these variables separately is because the estimated values of the respective local error
718 for mechanical (σ^* and p_0') and water retention responses (S_r and S_{R0}^*) can have different
719 magnitudes. Hence, it is important for an efficient integration of a problem involving
720 unsaturated soils that when substepping integration schemes with automatic error
721 control are used, the error measure *REL* is estimated accounting for all major sources
722 of error, and for unsaturated soils these should include the local error arising during the
723 numerical integration of both mechanical and water retention constitutive relations. In
724 the two substepping integration schemes presented here, this measure of relative local

725 error REL is estimated by taking the difference between the higher order accurate and
 726 the lower order accurate approximations for σ^* , p_0' , S_r and s_{R0}^* . Each of these
 727 differences is then divided by the corresponding higher order approximation (indicated
 728 by a hat in Equation 65). For the modified Euler with substepping this corresponds to
 729 the difference between second order accurate modified Euler and first order accurate
 730 forward Euler. For the RKDP5 with substepping, REL is calculated from fourth and
 731 fifth Runge-Kutta-Dormand-Prince approximations.

732 Equivalently to what is proposed in Sloan et al. (2001) for saturated soils, REL takes
 733 the maximum of these four relative measures of the step/substep error as a way to bound
 734 the local error:

$$735 \quad REL = \max \left\{ \frac{\left[\left(\hat{\sigma}^* - \sigma^* \right)^T \left(\hat{\sigma}^* - \sigma^* \right) \right]^{1/2}}{\left[\left(\hat{\sigma}^* \right)^T \left(\hat{\sigma}^* \right) \right]^{1/2}}, \frac{|\hat{p}_0' - p_0'|}{\hat{p}_0'}, \frac{|\hat{S}_r - S_r|}{\hat{S}_r}, \frac{|\hat{s}_{R0}^* - s_{R0}^*|}{\hat{s}_{R0}^*} \right\} \quad (65)$$

736 4.1. Modified Euler with substepping

737 Given a pseudo-time step/substep ${}^i(\Delta T)$ with $0 < {}^i(\Delta T) \leq 1$, the forward Euler and
 738 modified Euler updates for σ^* , p_0' , S_r and s_{R0}^* are described in the following by adopting
 739 the Butcher tableau (Dormand and Prince, 1980). The coefficients for the two methods
 740 are summarised in Table 1. The subscripts i and $i+1$ denote quantities evaluated at
 741 pseudo-times iT and ${}^{i+1}T = {}^iT + {}^i(\Delta T)$ respectively:

$$742 \quad {}^{i+1}s = {}^is + {}^i\Delta s \quad (66)$$

$$743 \quad {}^{i+1}v = {}^iv \exp(-{}^i\Delta \epsilon_v) \quad (67)$$

$$744 \quad {}^{i+1}s^* = {}^{i+1}s \frac{{}^{i+1}v - 1}{{}^{i+1}v} \quad (68)$$

$$745 \quad {}^{i+1}\sigma^* = {}^i\sigma^* + \sum_{k=1}^{n_s} k b^k \Delta \sigma^* \quad (69)$$

$$746 \quad {}^{i+1}p_0' = {}^i p_0' + \sum_{k=1}^{n_s} {}^k b^k \Delta p_0' \quad (70)$$

$$747 \quad {}^{i+1}S_r = {}^i S_r + \sum_{k=1}^{n_s} {}^k b^k \Delta S_r \quad (71)$$

$$748 \quad {}^{i+1}S_{R0}^* = {}^i S_{R0}^* + \sum_{k=1}^{n_s} {}^k b^k \Delta S_{R0}^* \quad (72)$$

749 where the coefficients ${}^k b$ are summarised in Table 1, n_s is the number of stages of the
750 integration scheme, and

$$751 \quad \left. \begin{aligned} & {}^k \Delta S^* = {}^{i+1}S^* - {}^i S^* \\ & {}^k \Delta \boldsymbol{\sigma}^* = {}^k \mathbf{D}_e {}^i \Delta \boldsymbol{\varepsilon} - {}^k \Delta \lambda_M {}^k \mathbf{D}_e {}^k \mathbf{a}_M \\ & {}^k \Delta p_0' = {}^k \Delta \lambda_M {}^k B_M \\ & {}^k \Delta S_r = -{}^k \Delta \lambda_R a_R \\ & {}^k \Delta S_{R0}^* = {}^k \Delta \lambda_R {}^k B_R \\ & {}^i \Delta S = {}^i (\Delta T) \Delta s \\ & {}^i \Delta \boldsymbol{\varepsilon} = {}^i (\Delta T) \Delta \boldsymbol{\varepsilon} \end{aligned} \right\} \text{for } k = 1, \dots, n_s \quad (73)$$

752 where \mathbf{D}_e , \mathbf{a}_M , $\Delta \lambda_M$, $\Delta \lambda_R$, B_M and B_R are evaluated at k using:

$$753 \quad \left. \begin{aligned} & {}^k \hat{s} = {}^i s + \sum_{j=1}^{k-1} {}^{kj} a^j ({}^i \Delta T) \Delta s \\ & {}^k \hat{v} = {}^i v \exp \left(- \sum_{j=1}^{k-1} {}^{kj} a^j ({}^i \Delta T) \Delta \varepsilon_v \right) \\ & {}^k \hat{s}^* = {}^k \hat{s} \frac{{}^k \hat{v} - 1}{{}^k \hat{v}} \\ & {}^k \hat{\boldsymbol{\sigma}}^* = {}^i \boldsymbol{\sigma}^* + \sum_{j=1}^{k-1} {}^{kj} a^j \Delta \boldsymbol{\sigma}^* \\ & {}^k \hat{p}_0' = {}^i p_0' + \sum_{j=1}^{k-1} {}^{kj} a^j \Delta p_0' \\ & {}^k \hat{S}_r = {}^i S_r + \sum_{j=1}^{k-1} {}^{kj} a^j \Delta S_r \\ & {}^k \hat{S}_{R0}^* = {}^i S_{R0}^* + \sum_{j=1}^{k-1} {}^{kj} a^j \Delta S_{R0}^* \end{aligned} \right\} \text{for } k = 1, \dots, n_s \quad (74)$$

754 and the coefficients ^{kj}a are summarised in Table 1.

755 Lloret-Cabot et al. (2016) demonstrate, for critical state models for saturated soils, the
 756 importance of ensuring that the update of v is consistent (i.e. at the same integration
 757 portion of $\Delta\varepsilon$) with the update of effective stresses σ' and hardening parameter p_0' . An
 758 equivalent logic applies to integration of critical state models for unsaturated soils that
 759 account for mechanical and water retention behaviour where not only v , but also S_r
 760 needs to be updated rigorously (i.e. now at the same integration portion of both $\Delta\varepsilon$ and
 761 Δs) with the update of σ^* , s^* , p_0' and s_{R0}^* (Equation 74).

762 Strain-driven formulations allow for the exact computation of specific volume, matric
 763 suction and modified suction at the end of the step/substep because it is possible to
 764 integrate them analytically over $^i\Delta T$ to find the precise values of v , s and s^* at $i+1$. The
 765 corresponding second order accurate updates for σ^* , p_0' , S_r and s_{R0}^* are respectively
 766 given by Equations 69-72 where $^1\Delta\sigma^*$, $^1\Delta p_0'$, $^1\Delta S_r$ and $^1\Delta s_{R0}^*$ correspond to the
 767 forward Euler increments and, $^2\Delta\sigma^*$, $^2\Delta p_0'$, $^2\Delta S_r$ and $^2\Delta s_{R0}^*$ are computed using first
 768 order updated variables (see Equations 73 and 74). If the step/substep is accepted, the
 769 variables σ^* , p_0' , S_r and s_{R0}^* are updated using the higher order approximation (i.e. *local*
 770 *extrapolation* see Shampine, 1994).

771 Table 1. Coefficients for the forward Euler and modified Euler integration schemes
 772 (Dormand and Prince, 1980)

| $^k c$ | ^{kj}a | | | | | $^k \hat{b}$ (2 nd) | $^k b$ (1 st) |
|--------|----------|--|--|--|--|---------------------------------|---------------------------|
| 0 | | | | | | 1/2 | 1 |
| 1 | 1 | | | | | 1/2 | 0 |

773 4.2. Runge-Kutta-Dormand-Prince (RKDP) with substepping

774 The explicit Runge-Kutta-Dormand-Prince (RKDP) with substepping is applied here to
 775 integrate the mechanical and water retention relations of the GCM for STRPTH= 4, 5
 776 and 6. When applying this scheme to Equations 58-64, the same Equations 66-74 are
 777 obtained but, for this method, the coefficients $^k b$ and ^{kj}a correspond to those summarised
 778 in Table 2.

779 The RKDP scheme with substepping gives very accurate values for ${}^{i+1}\sigma^*$, ${}^{i+1}p_0'$, ${}^{i+1}S_r$
780 and ${}^{i+1}S_{R0}^*$ at the end of each step/substep, at the expense of additional evaluations of
781 the constitutive relations. In the absence of an analytical solution, these highly accurate
782 approximations are used as a *reference* to check the accuracy of lower order methods.

783 Table 2. Coefficients for the RKDP4 and RKDP5 integration schemes (Dormand and
784 Prince, 1980)

| ${}^k c$ | ${}^{kj} a$ | | | | | ${}^k \hat{b}$ (5 th) | ${}^k b$ (4 th) |
|----------|-------------|--------|----------|--------|--------|-----------------------------------|-----------------------------|
| 0 | | | | | | 19/216 | 31/540 |
| 1/5 | 1/5 | | | | | 0 | 0 |
| 3/10 | 3/40 | 9/40 | | | | 1000/2079 | 190/297 |
| 3/5 | 3/10 | -9/10 | 6/5 | | | -125/216 | -145/108 |
| 2/3 | 226/729 | -25/27 | 880/729 | 55/729 | | 81/88 | 351/220 |
| 1 | -181/270 | 5/2 | -266/297 | -91/27 | 189/55 | 5/56 | 1/20 |

785 5. VERIFICATION AND COMPUTATIONAL ASPECTS

786 The variation of the local error with the size of the integrated increments depends on
787 the order of local accuracy of the numerical method used. Based on this information,
788 Lloret-Cabot et al. (2016) propose a verification method for the numerical integration
789 of constitutive models for saturated soils. This verification strategy is especially
790 convenient for explicit substepping integration schemes, because it first checks the
791 expected behaviour of the error at the level of one single step/substep and it then checks
792 the theoretical response of the cumulative error over several substeps.

793 As demonstrated here, the same strategy can be adapted to study the behaviour of the
794 error in the numerical integration of models for unsaturated soils. In the development
795 presented hereafter, e refers to the error incurred by the numerical scheme in a single
796 substep (or step in the case of no substepping) and E is the cumulative error over a
797 number of substeps. Note that the error control in a substepping strategy only controls
798 the error in a single substep, with the aim of controlling the cumulative error over
799 several steps.

800 To study the behaviour of the local error when numerically integrating a model, it is
801 useful to compare the approximations given by the integration scheme against a
802 reference or, when possible, an analytical solution. Given that the GCM involves

803 mechanical and water retention behaviour, it is necessary to study the magnitude of the
804 error not only in the mechanical response (as shown in Lloret-Cabot et al. (2016) for
805 the saturated MCC) but also in the water retention response. Consequently, the
806 assessment of the error investigated here for the integration of the GCM will include
807 the relative error incurred in the approximated mechanical response (in terms of
808 Bishop's stresses σ^* and mechanical hardening parameter p_0') and the approximated
809 water retention response (in terms of degree of saturation S_r and a water retention
810 hardening parameter s_{R0}^*) when varying the size of $\Delta\varepsilon$, Δs or both. The relative error in
811 each of these variables in a single substep/step is computed as:

$$812 \quad e_{\sigma^*} = \frac{\left\{ (\sigma_{ref}^* - \sigma^*)^T (\sigma_{ref}^* - \sigma^*) \right\}^{1/2}}{\left\{ (\sigma_{ref}^*)^T (\sigma_{ref}^*) \right\}^{1/2}} \quad (75)$$

$$813 \quad e_{S_r} = \frac{|S_{rref} - S_r|}{S_{rref}} \quad (76)$$

$$814 \quad e_{p_0'} = \frac{|p_{0ref}' - p_0'|}{p_{0ref}'} \quad (77)$$

$$815 \quad e_{s_{R0}^*} = \frac{|s_{R0ref}^* - s_{R0}^*|}{s_{R0ref}^*} \quad (78)$$

816 where the subscript *ref* indicates a reference solution (or, when available, analytical).

817 5.1. Relative error in a single-step

818 Two numerical tests are carried out to study how the error in σ^* , S_r , p_0' and s_{R0}^*
819 propagates during a single integration step (i.e. with no substepping) using the second
820 order modified Euler (ME2) and the fifth order Runge-Kutta-Dormand-Prince
821 (RKDP5) integration schemes. Both tests assume axisymmetric conditions and consider
822 an initial unsaturated stress state lying on both mechanical and wetting retention yield
823 curves, at zero deviatoric stress. The soil constants and initial state considered in all the
824 simulations are summarised in Tables 3 and 4, respectively. This initial state gives

825 initial values of specific volume and degree of saturation $v = 2.20$, $S_r = 0.65$. Further
 826 details on model parameters and initial state of GCM are found in Lloret-Cabot et al.
 827 (2017). The tolerance associated with yield surface intersections and the correction of
 828 the stresses back to the yield curve, $FTOL$, is assumed equal to 10^{-12} .

829 Table 3. Values of soil constants for the GCM simulations for Tests A, B and C

| | | | | |
|------------------|-----------------|--------------|--------------------|------------------|
| $\lambda = 0.15$ | $\kappa = 0.02$ | $N = 2.73$ | $R = 1.4$ | $M = 1.20$ |
| $N^* = 2.90$ | $k_1 = 0.70$ | $k_2 = 0.80$ | $\lambda_s = 0.12$ | $\nu = 0.33$ (*) |

830 (*) where ν is the Poisson's ratio (tangent and secant values of shear modulus were calculated from the corresponding tangent and
 831 secant values of bulk modulus by assuming a constant value of Poisson's ratio.

832 Table 4. Initial state for GCM simulations for Tests A and B (see the Appendix A)

| | | |
|--------------------|-------------|----------------------|
| $p^* = 200$ kPa | $q = 0$ kPa | $p_0^* = 200$ kPa |
| $s^* = 109.09$ kPa | -- | $s_1^* = 109.09$ kPa |

833 The reason for considering this type of initial state (with $p^* = p_0^*$ and $s^* = s_1^*$) is because
 834 when positive increments of strain (loading) and/or decrements of matric suction
 835 (wetting) are applied from the assumed initial state, simultaneous yielding on the
 836 mechanical and wetting retention yield curves (STRPTH=5) is activated which
 837 corresponds to the desired situation in which the numerical approximation of all four
 838 variables investigated contain some amount of error.

839 The first numerical test (Test A) studies the variation of the error for given finite equal
 840 variations of axial strain and radial strain $\Delta\varepsilon_a = \Delta\varepsilon_r \approx \Delta\varepsilon_v/3$ (where $\Delta\varepsilon_v$ is the increment
 841 of volumetric strain) with no variation of suction (i.e. isotropic straining at constant
 842 suction). The second test (Test B) studies the error response for a combined axial strain
 843 increment $\Delta\varepsilon_a$ (with no radial strains, $\Delta\varepsilon_r$) and a finite decrement of suction $-\Delta s$ (i.e.
 844 axial straining under wetting).

845 Test A computes the error by comparing the numerical approximation against the
 846 corresponding analytical solution. This comparison provides, hence, a clear and
 847 unambiguous interpretation of the error results. Conversely, Test B compares the
 848 numerical approximation against a reference solution (obtained by using the RKDP
 849 scheme with substepping and very stringent tolerances). In the two numerical tests
 850 presented, the size of the assumed input increments of strains and suction are varied to
 851 study how such variation in size influences the error in the solution. For Test A, the

852 volumetric strain increment size analysed varies from $\Delta\varepsilon_v = 10^{-06}$ to 0.1 (with $\Delta s = 0$).
 853 For Test B, the increment sizes varied from $\Delta\varepsilon_a = 10^{-06}$ and $\Delta s = -10^{-06}$ kPa to $\Delta\varepsilon_a =$
 854 0.01 and $\Delta s = -0.01$ kPa (keeping $\Delta\varepsilon_r = 0$).

855 Accuracy in each numerical method is assessed by plotting the error in σ^* , S_r , p_0' and
 856 s_{10}^* against the size of the input of strain or suction variations using logarithmic scales.
 857 This form of plotting the error results provides a first form of verification of an
 858 integration scheme, because the gradient obtained for the best-fitted straight line
 859 through a particular set of error results (i.e. all belonging to approximations from the
 860 same integration scheme) should be in correspondence with the order of accuracy of
 861 the numerical integration method (Lloret-Cabot et al., 2016).

862 Figures 7 and 8 illustrate the behaviour of the relative error for Tests A and B
 863 respectively, for a single step. Each figure is in four parts. The response of the relative
 864 error for the mechanical behaviour is shown in Parts (a) and (c), in terms of Bishop's
 865 stress σ^* and mechanical hardening parameter p_0' , respectively. Parts (b) and (d) show
 866 the response of the relative error for the water retention behaviour in terms of degree of
 867 saturation S_r and wetting retention hardening parameter s_{10}^* , respectively. In the figures,
 868 symbols indicate the computed relative error and the dashed lines indicate the best-
 869 fitted straight line through the computed relative error for the same numerical method.
 870 Typical error results for Test A when using the ME2 and RKDP5 schemes, respectively,
 871 are summarised in Tables 5 and 6.

872 Table 5. Typical relative error values in Bishop's stress σ^* , degree of saturation S_r ,
 873 mechanical hardening parameter p_0' and wetting retention hardening parameter s_{10}^* for
 874 a single elasto-plastic isotropic loading step at constant suction for the modified Euler
 875 with substepping (ME2) considering $STOL = 1$.

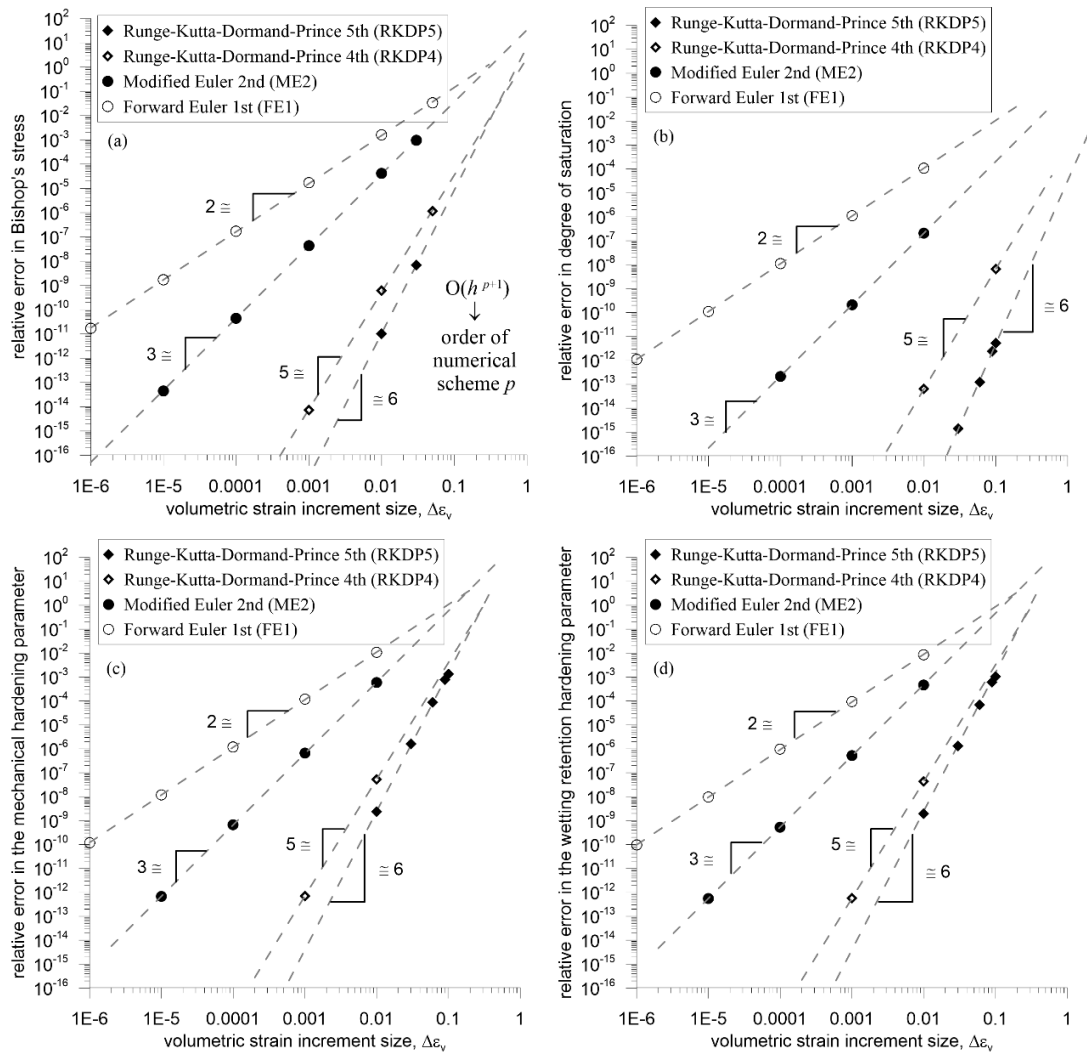
| $\Delta\varepsilon_v$ | Error in σ^* | Error in S_r | Error in p_0' | Error in s_{10}^* |
|-----------------------|------------------------|------------------------|------------------------|------------------------|
| $1 \cdot 10^{-06}$ | $< 1.0 \cdot 10^{-15}$ |
| $1 \cdot 10^{-05}$ | $4.50 \cdot 10^{-14}$ | $< 1.0 \cdot 10^{-15}$ | $6.74 \cdot 10^{-13}$ | $5.41 \cdot 10^{-13}$ |
| $1 \cdot 10^{-04}$ | $4.37 \cdot 10^{-11}$ | $2.15 \cdot 10^{-13}$ | $6.72 \cdot 10^{-10}$ | $5.38 \cdot 10^{-10}$ |
| $1 \cdot 10^{-03}$ | $4.35 \cdot 10^{-08}$ | $2.14 \cdot 10^{-10}$ | $6.64 \cdot 10^{-07}$ | $5.31 \cdot 10^{-07}$ |
| $1 \cdot 10^{-02}$ | $4.10 \cdot 10^{-05}$ | $2.09 \cdot 10^{-07}$ | $5.89 \cdot 10^{-04}$ | $4.72 \cdot 10^{-04}$ |
| $1 \cdot 10^{-01}$ | $1.39 \cdot 10^{-02}$ | $9.00 \cdot 10^{-05}$ | $1.30 \cdot 10^{-01}$ | $1.18 \cdot 10^{-01}$ |

876 Table 6. Typical relative error values in Bishop's stress σ^* , degree of saturation S_r ,
877 mechanical hardening parameter p_0' and wetting retention hardening parameter s_{10}^* for
878 a single elasto-plastic isotropic loading step at constant suction for Runge-Kutta-
879 Dormand-Prince with substepping (RKDP5) considering $STOL=1$.

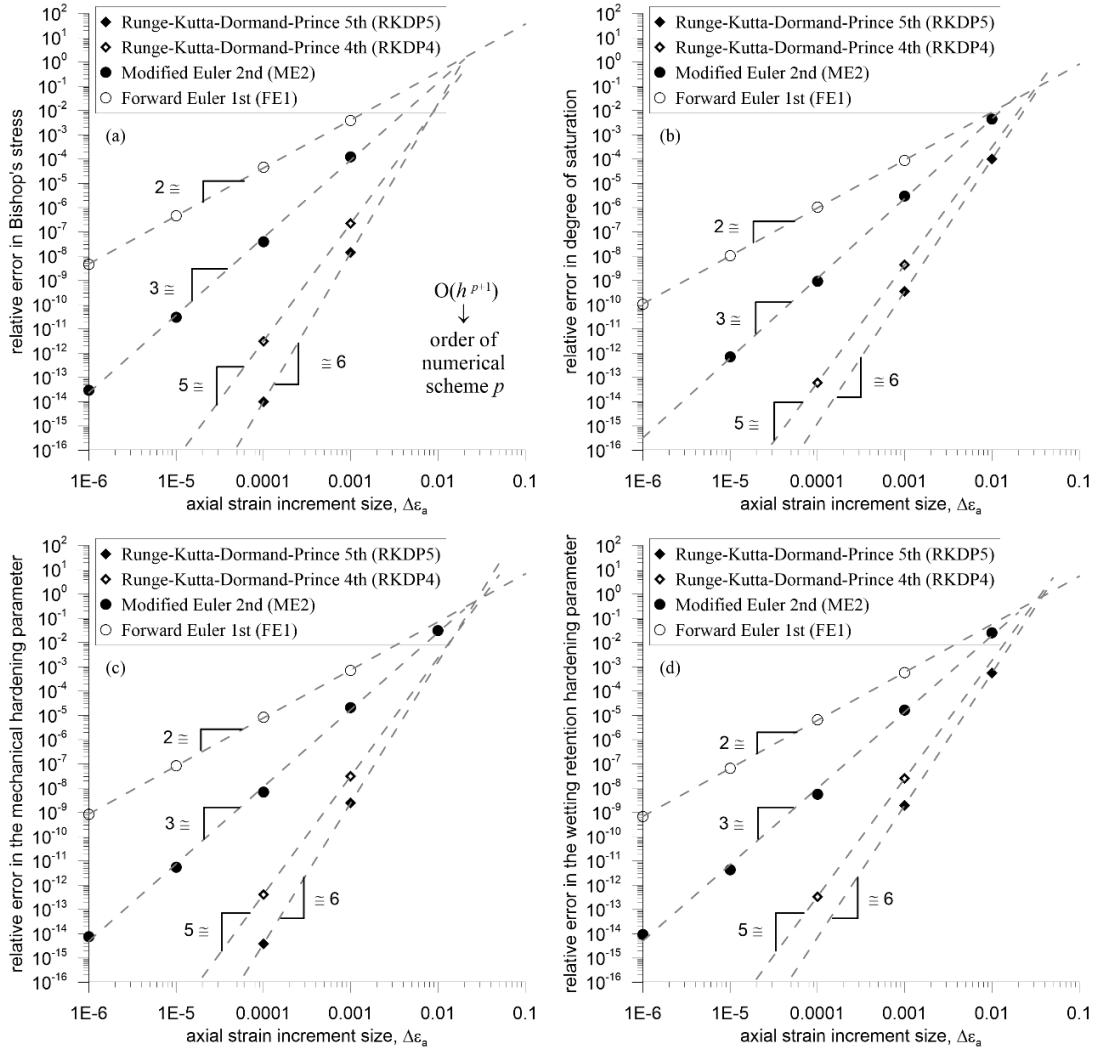
| $\Delta\varepsilon_v$ | Error in σ^* | Error in S_r | Error in p_0' | Error in s_{10}^* |
|-----------------------|------------------------|------------------------|------------------------|------------------------|
| $1 \cdot 10^{-06}$ | $< 1.0 \cdot 10^{-15}$ |
| $1 \cdot 10^{-05}$ | $< 1.0 \cdot 10^{-15}$ |
| $1 \cdot 10^{-04}$ | $< 1.0 \cdot 10^{-15}$ |
| $1 \cdot 10^{-03}$ | $< 1.0 \cdot 10^{-15}$ |
| $1 \cdot 10^{-02}$ | $1.02 \cdot 10^{-11}$ | $< 1.0 \cdot 10^{-15}$ | $2.39 \cdot 10^{-09}$ | $1.91 \cdot 10^{-09}$ |
| $1 \cdot 10^{-01}$ | $6.94 \cdot 10^{-06}$ | $5.31 \cdot 10^{-12}$ | $1.33 \cdot 10^{-03}$ | $1.06 \cdot 10^{-03}$ |

880 The respective gradients of each best-fitted straight line plotted in both figures match
881 the expected order of accuracy of the method, suggesting that both substepping schemes
882 work correctly at a single step/substep level. In particular, for both tests, approximate
883 gradients of 6 are obtained when best-fitting a straight line through the computed error
884 values in σ^* , S_r , p_0' and s_{10}^* corresponding to the RKDP5 method and approximate
885 gradients of 3 are obtained when best-fitting a straight line through the computed error
886 values in σ^* , S_r , p_0' and s_{10}^* corresponding to the ME2 method. Note that, for
887 completeness, Figures 7 and 8 also include the best-fitted lines for the computed error
888 values for the single-step first order forward Euler (gradient 2) and single-step fourth
889 order Runge-Kutta-Dormand-Prince (gradient 5) integration schemes, in addition to the
890 error results for ME2 and RKDP5.

891 The results in Figures 7 and 8 show that the specific values of the local relative error
892 incurred in each variable considered during the numerical integration, differ in each
893 numerical test considered. In particular, the variation of the position of each best-fitted
894 line (i.e. intercept) differs in each test and for each variable considered. This behaviour
895 justifies the decision of treating separately the local error from mechanical (i.e. σ^* and
896 p_0') and water retention (i.e. S_r and s_{10}^*) responses.



897 Figure 7. Relative error for single-step explicit integration schemes against volumetric
 898 strain increment size for a single elasto-plastic isotropic strain increment at constant
 899 suction: (a) Bishop's stress σ^* ; (b) degree of saturation S_r ; (c) mechanical hardening
 900 parameter p_0' ; (d) water retention hardening parameter s_{10}^* .



901 Figure 8. Relative error for single-step explicit integration schemes against axial strain
 902 increment size for a single elasto-plastic axial strain increment (at constant radial strain)
 903 under wetting: (a) Bishop's stress σ^* ; (b) degree of saturation S_r ; (c) mechanical
 904 hardening parameter p_0' ; (d) water retention hardening parameter s_{10}^* .

905 5.2. Substepping analysis: cumulative relative error

906 Once a substepping integration scheme has been verified at a single step level, the
 907 verification process should study the numerical performance over several substeps. In
 908 this context, Lloret-Cabot et al. (2016) propose to study the behaviour of the cumulative
 909 relative error E incurred in an integration scheme when the substepping is active.
 910 Assuming no cancellation, the addition of each amount of relative error e incurred in
 911 each substep corresponds to the cumulative relative error E . Lloret-Cabot et al. (2016)
 912 show that $e \cong ch^{p+1}$ (where h is the substep size, p is the order of the integration scheme

913 and c is simply a constant that fixes the position of an error line for a single step/substep
914 in the $\ln e:\ln h$ plane) and that, for n equal-sized substeps of size h , $E \cong nch^{p+1} = Hch^p$
915 (where H is the size of the total increment integrated i.e. $H=hn$). This means that the
916 final cumulative error (incurred during the integration of a given total increment H)
917 approximately lies on a straight line when plotted against the substep size h in a log-log
918 scale, having gradient 2 for the ME2 and 5 for RKDP5 with substepping schemes.
919 Similarly to the error lines for a single step/substep, the intercept of a cumulative error
920 line is Hc (as $E \cong Hch^p$) and, hence, the distance between the best-fitted straight line for
921 the single-step error and a cumulative error line for an increment involving many
922 substeps can be checked at a particular step/substep size h (Lloret-Cabot et al. 2016).

923 The numerical integration of Tests A and B is performed again using the ME2 and
924 RKDP5 schemes with substepping but now imposing values of $STOL$ small enough to
925 activate the substepping. In the analyses presented next, the maximum number of
926 substeps is limited to 10^{+06} and the values for $STOL$ vary from 1 to 10^{-08} .

927 The study of the numerical performance of each integration scheme is in two parts. An
928 investigation on how the errors are accumulated over the substeps integrated is
929 presented first, to check that the computed cumulative error is consistent with that of
930 the numerical method used. The performance maps proposed in Lloret-Cabot et al.
931 (2016) are presented in the second part of the analysis to check that the substepping
932 integration performs correctly. Without loss of generalisation, the first part of the
933 analysis is carried out only for Test A. The study of the performance maps, on the other
934 hand, is carried out for both numerical tests.

935 The different values of $STOL$ considered (from 1 to 10^{-08}) together with the accumulated
936 contributions of relative error at each substep are illustrated in Figures 9 and 10 for the
937 ME2 and RKDP5 schemes with substepping, respectively. Tables 7 and 8 present
938 typical values of cumulative relative error for ME2 and RKDP5 substepping schemes,
939 respectively, during the numerical integration of a volumetric strain increment of 0.1
940 for $STOL = 10^{-02}$, 10^{-04} , 10^{-06} and 10^{-08} (Test A). In the tables, the total number of
941 substeps required in the algorithm is indicated by TS whereas the total number of failed
942 substeps (substeps requiring a further subdivision in size) is indicated by TF. No drift
943 correction iterations were necessary in Test A.

944 Table 7. Typical cumulative relative error values in Bishop's stress σ^* , degree of
 945 saturation S_r , mechanical hardening parameter p_0' and wetting retention hardening
 946 parameter s_{10}^* for an elasto-plastic isotropic strain increment of $\Delta\varepsilon_v = 0.1$ at constant
 947 suction for the modified Euler with substepping (ME2) considering different values of
 948 $STOL$.

| $STOL$ | Error in σ^* | Error in S_r | Error in p_0' | Error in s_{10}^* | TS | TF |
|--------------------|-----------------------|-----------------------|-----------------------|-----------------------|-------|----|
| $1 \cdot 10^{-02}$ | $2.96 \cdot 10^{-04}$ | $1.44 \cdot 10^{-06}$ | $4.45 \cdot 10^{-03}$ | $3.57 \cdot 10^{-03}$ | 11 | 2 |
| $1 \cdot 10^{-04}$ | $2.79 \cdot 10^{-06}$ | $1.32 \cdot 10^{-08}$ | $4.45 \cdot 10^{-05}$ | $3.56 \cdot 10^{-05}$ | 114 | 3 |
| $1 \cdot 10^{-06}$ | $2.78 \cdot 10^{-08}$ | $1.31 \cdot 10^{-10}$ | $4.46 \cdot 10^{-07}$ | $3.57 \cdot 10^{-07}$ | 1141 | 4 |
| $1 \cdot 10^{-08}$ | $2.78 \cdot 10^{-10}$ | $1.31 \cdot 10^{-12}$ | $4.46 \cdot 10^{-09}$ | $3.57 \cdot 10^{-09}$ | 11416 | 5 |

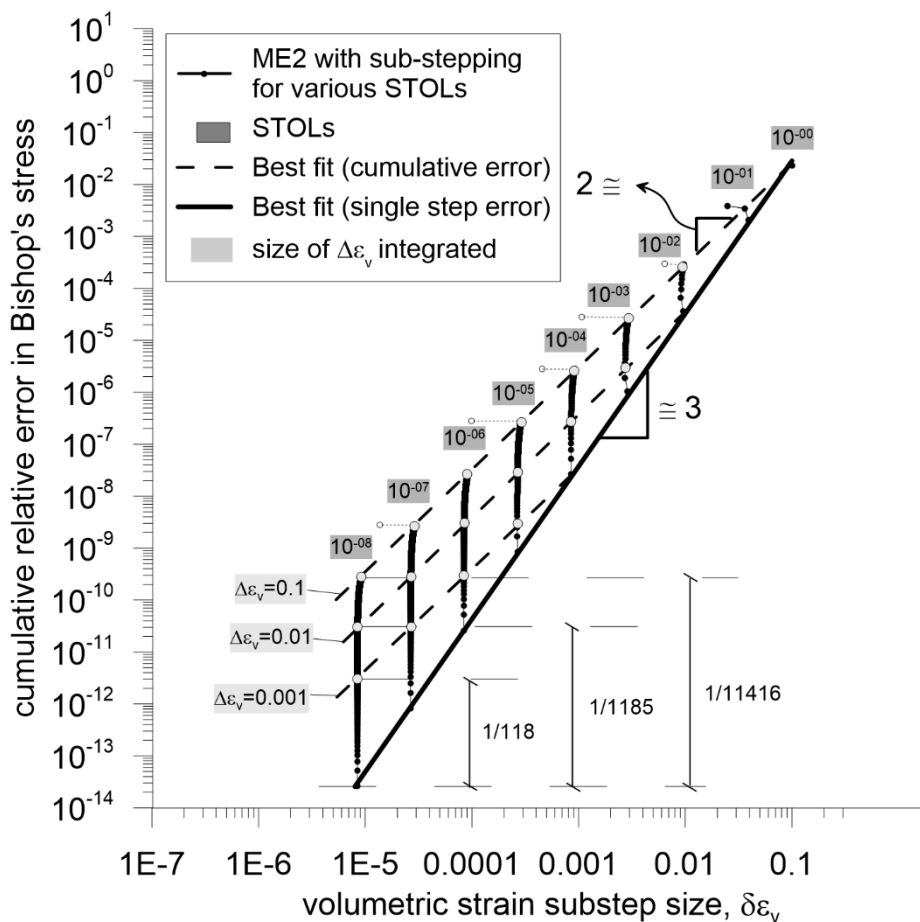
949 Table 8. Typical cumulative relative error values in Bishop's stress σ^* , degree of
 950 saturation S_r , mechanical hardening parameter p_0' and wetting retention hardening
 951 parameter s_{10}^* for an elasto-plastic isotropic strain increment of $\Delta\varepsilon_v = 0.1$ at constant
 952 suction for the Runge-Kutta-Dormand-Prince with substepping (RKDP5) considering
 953 different values of $STOL$.

| $STOL$ | Error in σ^* | Error in S_r | Error in p_0' | Error in s_{10}^* | TS | TF |
|--------------------|-----------------------|-----------------------|-----------------------|-----------------------|----|----|
| $1 \cdot 10^{-02}$ | $6.94 \cdot 10^{-06}$ | $5.30 \cdot 10^{-12}$ | $1.33 \cdot 10^{-03}$ | $1.06 \cdot 10^{-03}$ | 1 | 0 |
| $1 \cdot 10^{-04}$ | $3.95 \cdot 10^{-07}$ | $1.22 \cdot 10^{-13}$ | $8.87 \cdot 10^{-05}$ | $7.10 \cdot 10^{-05}$ | 2 | 2 |
| $1 \cdot 10^{-06}$ | $1.07 \cdot 10^{-09}$ | $1.24 \cdot 10^{-15}$ | $2.72 \cdot 10^{-07}$ | $2.17 \cdot 10^{-07}$ | 6 | 2 |
| $1 \cdot 10^{-08}$ | $8.38 \cdot 10^{-12}$ | $1.24 \cdot 10^{-15}$ | $2.16 \cdot 10^{-09}$ | $1.73 \cdot 10^{-09}$ | 16 | 2 |

954 The form of plotting the results shown in Figures 9 and 10 is particularly convenient to
 955 study how the cumulative relative error increases as the integration progresses
 956 (indicated by a series of data points forming a near vertical path in the figure) for various
 957 values of $STOL$. During a typical substepping integration of a prescribed volumetric
 958 strain increment $\Delta\varepsilon_v$ with n substeps, the relative error incurred in each of these substeps
 959 (all fulfilling the imposed $STOL$) accumulates over the substeps to give a value of the
 960 cumulative relative error (Lloret-Cabot et al., 2016). Figures 9 and 10 demonstrate that,
 961 indeed, the final values of cumulative relative error once the entire $\Delta\varepsilon_v$ has been
 962 integrated approximately lie on a straight line of gradient two for the ME2 with
 963 substepping and five for the RKDP5 with substepping (see dashed lines). This
 964 behaviour is true for all values of $STOL$ used (Figures 9 and 10). The vertical distance
 965 (measured upwards) from the best-fitted straight line for the single substep relative error
 966 (indicated by a thicker dark line) and one of these cumulative relative error lines (at a
 967 particular total increment size $\Delta\varepsilon_v$ and substep size $\delta\varepsilon_v$) corresponds to $1/n$ where n is

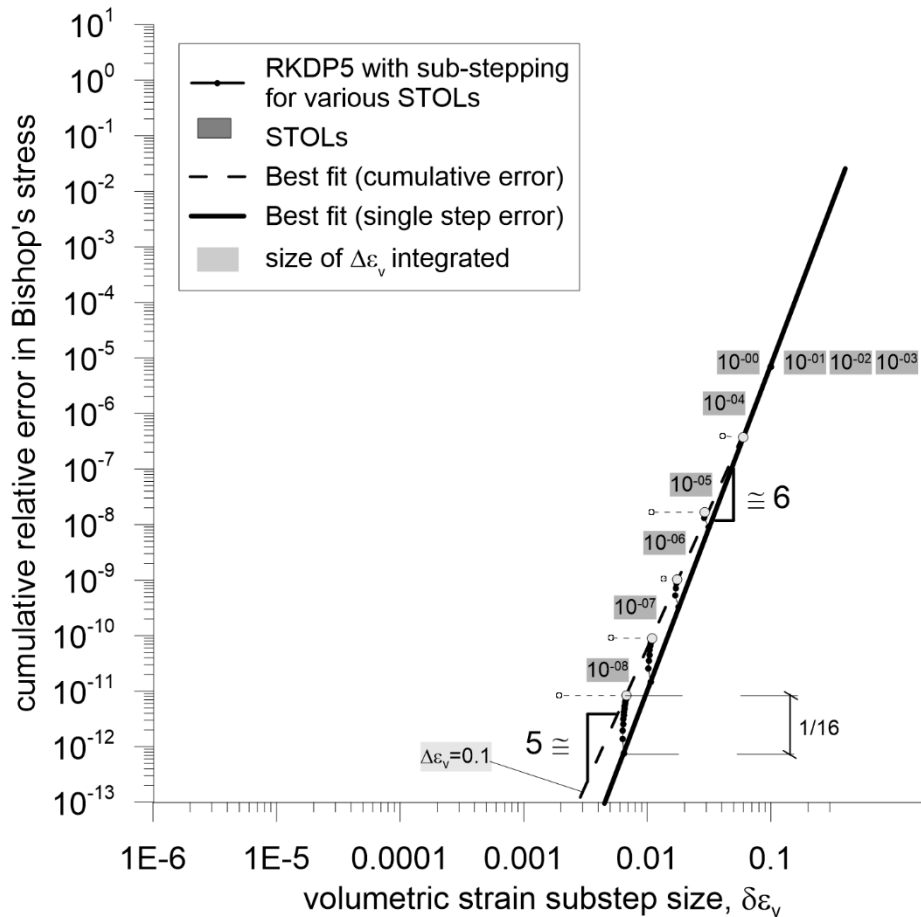
968 the number of substeps (Lloret-Cabot et al., 2016). This error response is illustrated in
 969 Figure 9 for three different sizes of volumetric strain increment (i.e. 0.001, 0.01 or 0.1),
 970 when using the ME2 with substepping and a value of $STOL=10^{-08}$. A total number of
 971 118 substeps are needed to integrate the volumetric strain increment size of 0.001, 1185
 972 for 0.01 and 11416 for 0.1. This response is less apparent when using the RKDP5
 973 scheme because of the small number of substeps typically required in this higher order
 974 method (Figure 10).

975 During the numerical integration of each $\Delta\varepsilon_v$ considered, the actual substep size being
 976 integrated is quite regular in the two substepping schemes considered as reflected by
 977 the approximately vertical paths traced by the cumulative error (Figures 9 and 10).



978

979 Figure 9. Cumulative relative error behaviour in Bishop's stresses for the modified
 980 Euler with substepping (ME2) integration scheme with different values of $STOL$ against
 981 strain increment size for an elasto-plastic isotropic loading increment.



982

983 Figure 10. Cumulative relative error behaviour in Bishop's stresses for the Runge-
 984 Kutta-Dormand-Prince with substepping (RKDP5) integration scheme with different
 985 values of *STOL* against strain increment size for an elasto-plastic isotropic loading
 986 increment.

987 Figure 11 shows the cumulative relative error (i.e. the accumulated relative error
 988 incurred over the number of substeps required to integrate a given increment of
 989 volumetric strain) for Bishop's stresses incurred in Test A plotted against *STOL* for
 990 each integrated size of volumetric strain increment $\Delta\epsilon_v$. Figure 12 plots the same
 991 cumulative relative error plotted against the number of substeps required for the
 992 integration of the entire strain increment. In these figures, part a) presents the results
 993 for the ME2 with substepping and part b) their RKDP5 substepping counterparts.

994 Inspection of Figure 11 shows how the influence of *STOL* in the relative error incurred
 995 in an individual substep $\delta\epsilon_v$ affects the cumulative relative error incurred in the
 996 integration of the entire $\Delta\epsilon_v$. As expected, a reduction in the values of *STOL* leads to a
 997 reduction in the relative error incurred in each individual substep of the computations

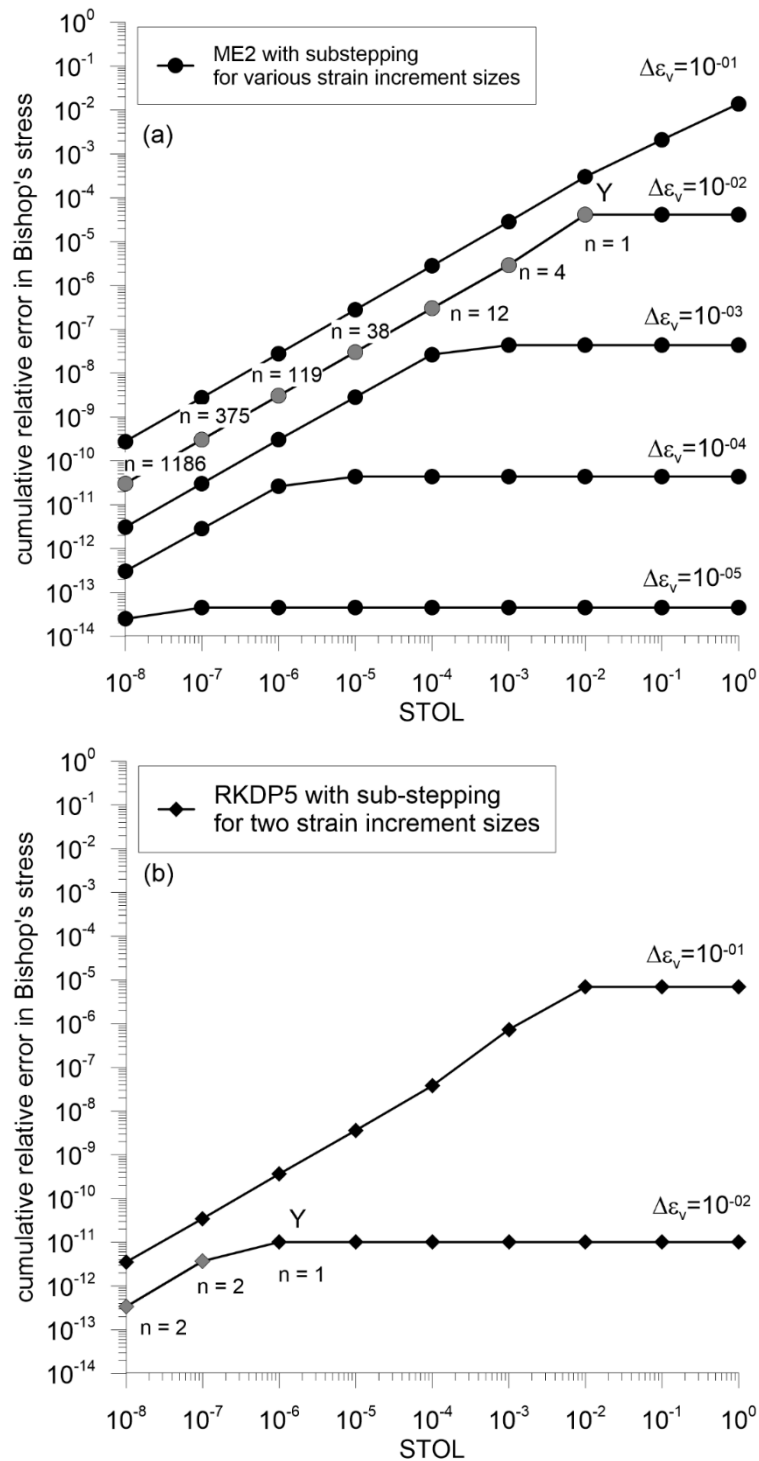
998 which, in turn, reduces the cumulative relative error. However, this reduction of the
999 cumulative relative error with decreasing $STOL$ is not apparent for small sizes of
1000 volumetric strain increment unless $STOL$ is less than a critical size (Figure 11).
1001 Similarly to what is observed in saturated soils (Lloret-Cabot et al., 2016), this is
1002 because for small increment sizes, even without substepping the difference between the
1003 two solutions of different order within the substepping scheme tends to be very small
1004 and, if it is less than the $STOL$ considered, the substepping strategy is not activated. For
1005 example, for a volumetric strain increment size of 10^{-02} , values of $STOL$ smaller than
1006 10^{-02} are required to activate the substepping strategy with the ME2 scheme (Point Y in
1007 Figure 11a). The RKDP5 with substepping, on the other hand, needs values of $STOL$
1008 smaller than 10^{-06} to activate substepping for a volumetric strain increment size of 10^{-2}
1009 (Point Y in Figure 11b). Figure 11a shows that for a volumetric strain increment size
1010 of 10^{-02} , 1186 substeps are required in the ME2 substepping scheme (with $STOL = 10^{-08}$)
1011 to reach a cumulative relative error of about 10^{-10} . In contrast, the RKDP5
1012 substepping scheme requires only 2 substeps to reach a similar (even substantially
1013 smaller) value of the cumulative relative error (see Figure 11b).

1014 As discussed earlier, the second order accurate modified Euler with substepping uses r
1015 $\cong 0.9(STOL/REL_n)^{1/2}$ and the fifth order accurate Runge-Kutta-Dormand-Prince with
1016 substepping uses $r \cong 0.9(STOL/REL_n)^{1/5}$. This means that the variation of the cumulative
1017 relative error with the number of substeps should follow, approximately, straight lines
1018 of gradient -2 for the ME2 integration scheme and, similarly, approximately straight
1019 lines of gradient -5 for the RKDP5 integration scheme as correctly illustrated in Figure
1020 12.

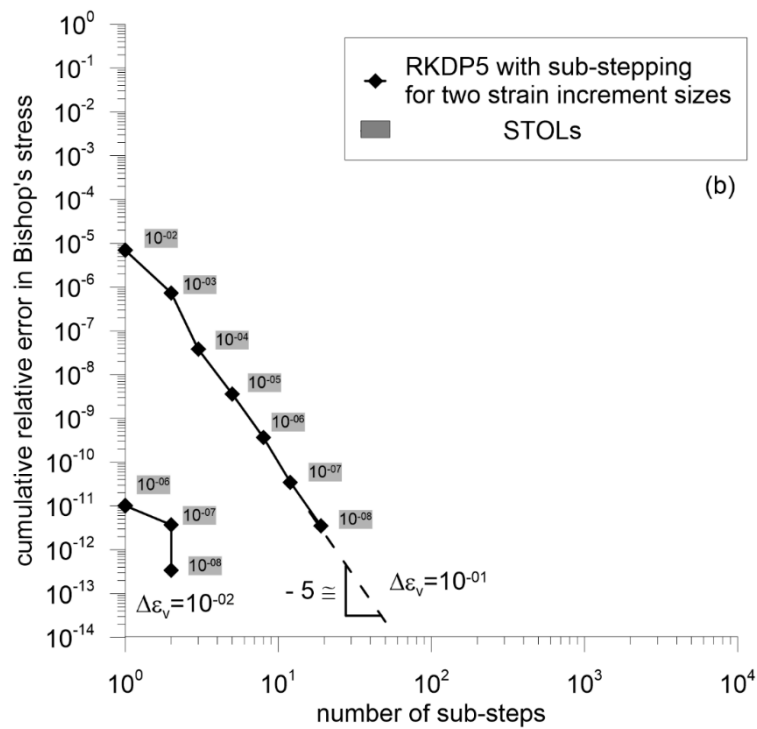
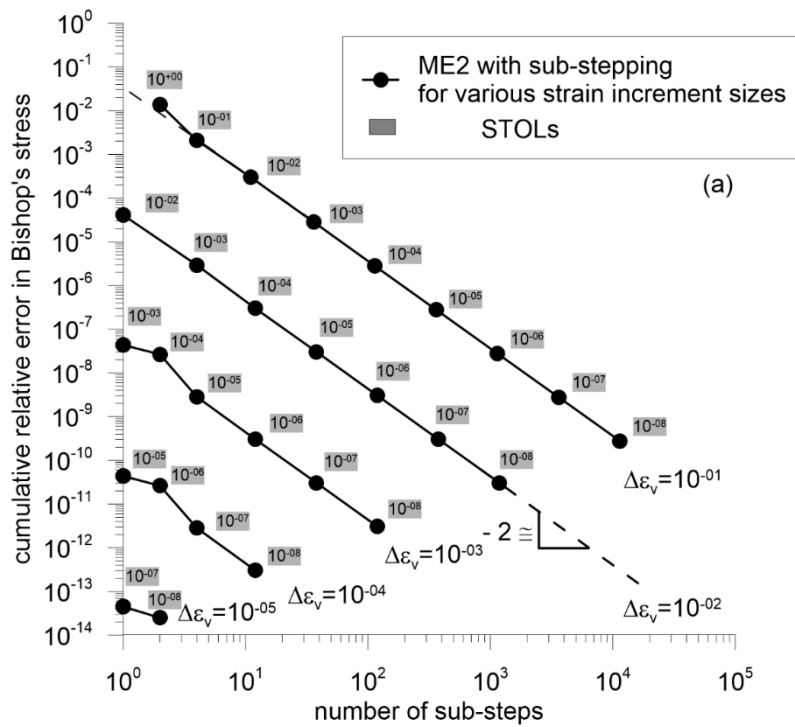
1021 The plots presented in Figure 11 and 12 correspond to the performance maps proposed
1022 in Lloret-Cabot et al. (2016) for saturated soils and its application is demonstrated here
1023 for unsaturated soils. The results obtained confirm that this specific form of plotting the
1024 computational outcomes from a substepping integration scheme is a powerful
1025 verification tool.

1026 Similar error responses to those just discussed for Figure 12 are also observed in Figure
1027 13 (Test B) for σ^* , S_r , p_0' and s_{10}^* when using the ME2 substepping integration scheme.
1028 Even in the case of not using an analytical solution to compute the relative error, the

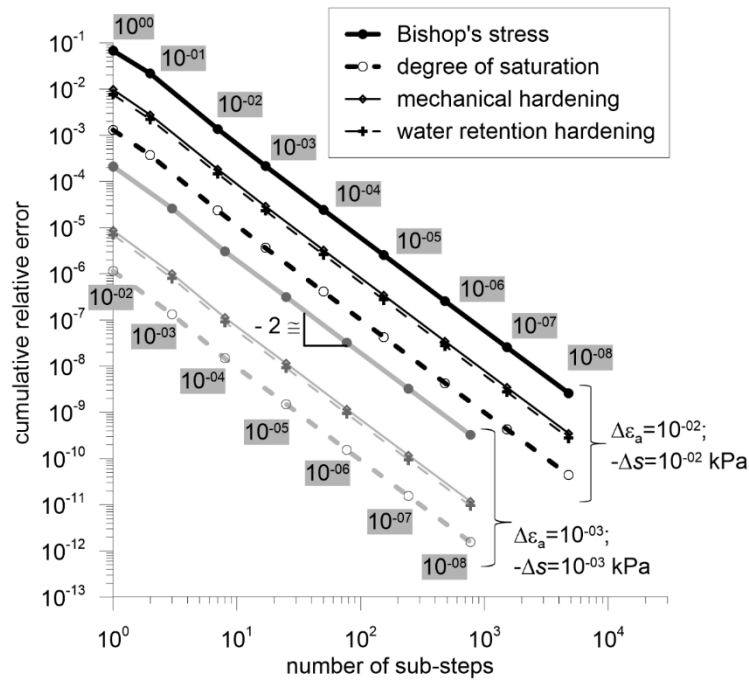
1029 error behaviour observed is consistent with that discussed when analytical solutions
 1030 were available.



1031 Figure 11. Cumulative relative error behaviour against *STOL* for an elasto-plastic
 1032 isotropic strain increment at constant suction: (a) Modified Euler with substepping
 1033 scheme (ME2); (b) Runge-Kutta-Dormand-Prince with substepping scheme (RKDP5).



1034 Figure 12. Cumulative relative error behaviour against number of substeps for an elasto-
 1035 plastic isotropic strain increment at constant suction: (a) Modified Euler with
 1036 substepping scheme (ME2); (b) Runge-Kutta-Dormand-Prince with substepping
 1037 scheme (RKDP5).



1038

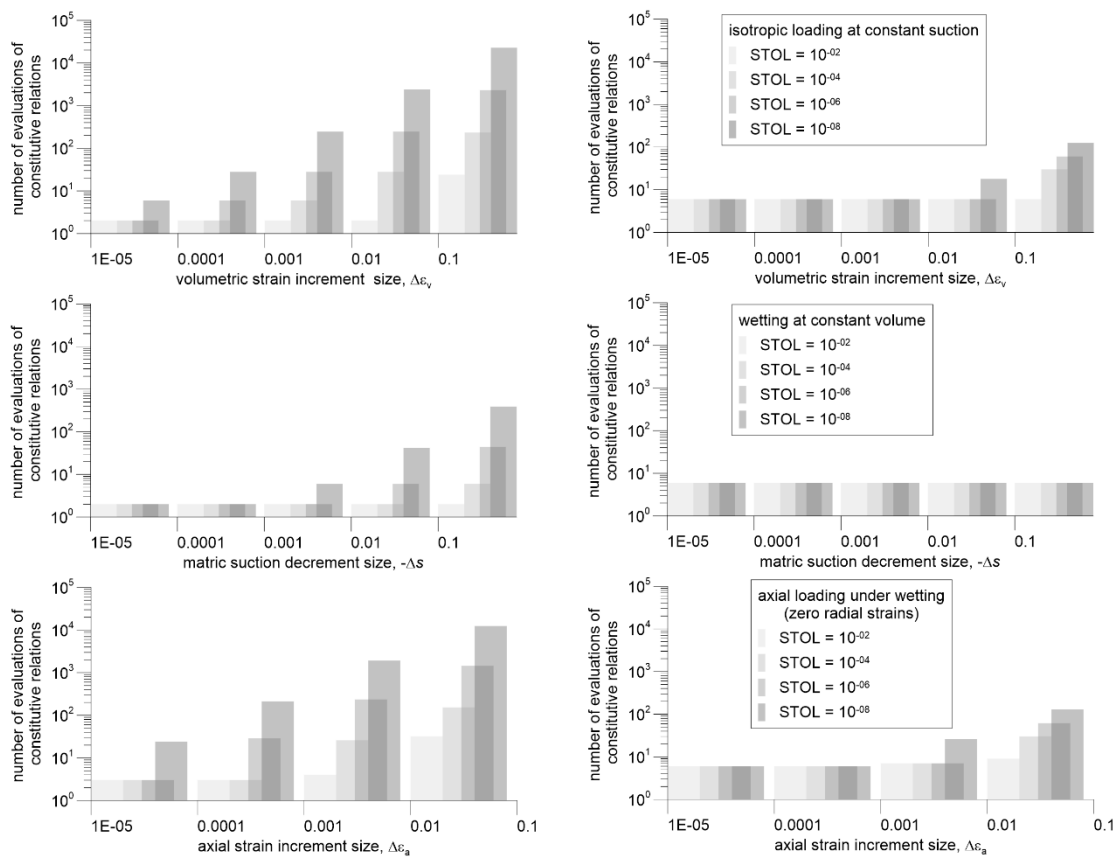
1039 Figure 13. Cumulative relative error behaviour against number of substeps for an elasto-
 1040 plastic axial strain increment (at constant radial strain) under wetting using the modified
 1041 Euler with substepping scheme (ME2).

1042 5.3. Computational cost and efficiency

1043 The simplicity of the numerical examples discussed above implies a very small CPU
 1044 time and, therefore, it is reasonable to assess the computational cost associated with
 1045 each example as proportional to the number of evaluations of the constitutive relations
 1046 that the substepping integration scheme employs to solve the problem (Sloan et al.,
 1047 2001). Equivalently to Lloret-Cabot et al. (2016), two evaluations of the constitutive
 1048 relations are required in the ME with substepping scheme and six are needed in the
 1049 RKDP substepping scheme. Additionally, the computational cost associated with any
 1050 rejected step as well as the computational cost associated with the number of iterations
 1051 used by the drift correction subroutine are also accounted for.

1052 Figure 14 shows the computational cost as a function of $STOL$ (i.e. $STOL= 10^{-02}$, 10^{-04} ,
 1053 10^{-06} and 10^{-08}), and the input increment size for the three numerical tests considered
 1054 earlier. Plots on the left correspond to the ME substepping scheme and plots on the right
 1055 show the approximations for the RKDP substepping scheme. A similar pattern to that

1056 found by Lloret-Cabot et al. (2016) when using the MCC model is also observed here
 1057 for the GCM. In general, from the two integration schemes investigated, the ME
 1058 substepping scheme requires a larger number of evaluations of the constitutive relations
 1059 (i.e. higher computational cost) to satisfy the value of $STOL$ when the sizes of the input
 1060 increment $\Delta\varepsilon_v$, $\Delta\varepsilon_a$, or Δs are large (and this observation is more pronounced when the
 1061 values of $STOL$ are more restrictive). In contrast, the RKDP substepping scheme is
 1062 more expensive for the smaller increment sizes. For intermediate increment sizes, the
 1063 optimal computational efficiency depends on the level of accuracy specified (RKDP
 1064 substepping scheme is most efficient for stringent tolerances whereas ME substepping
 1065 scheme is best for looser values of $STOL$).



1066

1067 Figure 14. Computational cost for different $STOL$ values against input increment sizes:
 1068 (left) modified Euler substepping scheme; (right) Runge-Kutta-Dormand-Prince
 1069 substepping scheme.

1070 6. CONCLUSIONS

1071 The complete formulation of the incremental constitutive relations of the Glasgow
1072 Coupled Model (GCM) has been presented for all possible elastic and elasto-plastic
1073 responses of the model, including transitions between saturated and unsaturated
1074 conditions. The formulation is expressed in terms of the increments of strain and
1075 increments of suction (i.e. strain-driven formulation) so that it is suitable for
1076 implementation into a finite element program, as it properly defines an initial value
1077 problem (IVP) when the initial stress state and the increments of strain and suction are
1078 known.

1079 A rigorous algorithm capable of identifying unambiguously which is the model
1080 response activated by a trial stress path has been developed after a small reformulation
1081 of the GCM that included the derivation of a useful closed-form expression for the
1082 mechanical yield curve in terms of degree of saturation. The correct identification of
1083 the intersection point, when a trial stress path moves from elastic to elasto-plastic
1084 behaviour, is achieved by using the Pegasus algorithm, widely used for solving the
1085 equivalent problem in explicit formulations for saturated soil models. The same strategy
1086 is applied to find the correct stress point at saturation and desaturation. A drift
1087 correction subroutine has been also presented to correct any potential deviation of the
1088 stress point at the end of each integrated elasto-plastic step/substep.

1089 Two explicit substepping formulations to integrate numerically the IVP defined by the
1090 initial state and the incremental relations of the GCM have been then presented,
1091 extending to unsaturated conditions the well-known explicit substepping integration
1092 schemes with automatic error control for saturated soils. These two substepping
1093 schemes presented correspond to the second order accurate modified Euler with
1094 substepping and the fifth order accurate Runge-Kutta-Dormand-Prince with
1095 substepping.

1096 In contrast to existing substepping formulations with automatic error control for
1097 saturated soils, which account only for the relative error associated with the integration
1098 of the mechanical part of the problem (i.e. stresses and mechanical hardening
1099 parameter), the extended substepping version with automatic error control presented in
1100 this paper accounts for the relative error incurred during the numerical integration of
1101 both the mechanical (stresses and mechanical hardening parameter) and water retention
1102 (degree of saturation and water retention hardening parameter) components of the

1103 problem. This is essential when applying substepping schemes to solve problems
1104 involving unsaturated soils, as this is what ensures an accurate and efficient integration.

1105 The correctness of the two substepping schemes presented is checked by investigating
1106 how the error over an individual step/substep and the cumulative error over multiple
1107 substeps propagate during the integration of two simple numerical tests, involving an
1108 isotropic straining at constant suction and a combined axial straining under wetting.
1109 The behaviour of the relative error observed when adopting a single-step integration in
1110 solving each of these tests is different for the mechanical and the water retention
1111 components of the problem, which confirms the importance of accounting separately
1112 for the different sources of error. The computational performance of the two
1113 substepping schemes is then checked by ensuring that the influence of the internal
1114 substepping tolerance *STOL* on the accuracy and the number of substeps used is as
1115 expected. The results obtained extend to unsaturated conditions the conclusions
1116 observed for saturated soils (Lloret-Cabot et al., 2016), confirming that the substepping
1117 methods proposed are capable of controlling the cumulative error (i.e. they satisfy the
1118 error tolerance *STOL* for all the cases considered).

1119 Finally, this investigation confirms that the importance of updating rigorously the
1120 specific volume in Cam Clay family models for saturated soils in substepping
1121 integration schemes extends also to the rigorous update of the degree of saturation in
1122 substepping integration schemes for critical state models for unsaturated soils.

1123 7. ACKNOWLEDGEMENTS

1124 This research has benefitted from the Marie-Skłodowska Curie project “*COUPLED*”
1125 funded from the H2020 programme of the EC (MSCA-IF-2015-706712). Support from
1126 the project “*TERRE*” (ETN-GA-2015-675762) of the EU is also acknowledged.

1127 8. APPENDICES

1128 8.1 Appendix A

1129 The Glasgow Coupled Model (GCM) predicts that isotropic stress states at the
1130 intersection of f_M and f_{WR} yield curves fall on unique unsaturated isotropic normal
1131 compression planar surfaces for v (in $v: \ln p^* : \ln s^*$ space) and also for S_r (in $S_r: \ln p^*$

1132 : $\ln s^*$ space). The forms of these two planar surfaces are (see also Lloret-Cabot et al.
1133 2017):

$$1134 \quad v = N^* - \lambda^* \ln p_0^* + k_1^* \ln s_1^* \quad (\text{A1})$$

$$1135 \quad S_r = \Omega^* - \lambda_s^* \ln s_1^* + k_2^* \ln p_0^* \quad (\text{A2})$$

1136 where N^* and Ω^* are their respective intercepts. The expressions of gradients λ^* , k_1^* ,
1137 λ_s^* and k_2^* are a combination of the soil parameters of the model (assuming $dS_r^e = 0$):

$$1138 \quad \lambda^* = \frac{\lambda - k_1 k_2 \kappa}{1 - k_1 k_2} \quad (\text{A3})$$

$$1139 \quad k_1^* = k_1 \frac{\lambda - \kappa}{1 - k_1 k_2} \quad (\text{A4})$$

$$1140 \quad \lambda_s^* = \frac{\lambda_s}{1 - k_1 k_2} \quad (\text{A5})$$

$$1141 \quad k_2^* = k_2 \frac{\lambda_s}{1 - k_1 k_2} \quad (\text{A6})$$

1142 Assuming $\kappa_s = 0$ (the gradient of elastic scanning curves in the $S_r : \ln s^*$ plane as defined
1143 in Wheeler et al., 2003), Lloret-Cabot et al. (2017) derives the following relationship
1144 between intercepts N , N^* and Ω^* :

$$1145 \quad \Omega^* = 1 - \frac{(N^* - N) \lambda_s}{k_1 (\lambda - \kappa)} \quad (\text{A7})$$

1146 Combining the above equations with the elastic relations of the GCM, it is possible to
1147 find the following expressions for v for any general stress state (Lloret-Cabot et al.,
1148 2017):

$$1149 \quad v = N^* - \lambda^* \ln p_0^* + k_1^* \ln s_1^* + \kappa \ln \left(\frac{p_0^*}{p^*} \right) \quad (\text{A8})$$

1150 Equation A8 can be used to calculate initial value of v when initial values of p^* , p_0^* and
 1151 s_1^* are known, together with the model parameters. Given that $dS_r^e = 0$, the initial value
 1152 of S_r can be also calculated from Equation A2 (Lloret-Cabot et al., 2017).

1153 8.2 Appendix B

1154 A more formalised description of the sequence of the steps followed by the algorithm
 1155 to determine which is the active response of the GCM is presented here for the most
 1156 general case of a stress point starting inside the three yield curves of the model and
 1157 potentially activating any of the six possible model responses. Any other case (i.e. stress
 1158 point starting on one or two yield curves) is a particular case of this one.

1159 (A) Compute *trial 1* assuming purely elastic behaviour.

1160 If *trial 1* is inside f_M, f_{DR} and f_{WR} then, elastic update from i to $i+1$ and *return*.

1161 If *trial 1* is outside f_M , outside f_R or outside both, yielding has occurred (note that
 1162 f_R is either f_{DR} or f_{WR}). Hence:

1163 If *trial 1* is outside only one yield curve (f_M or f_R).

1164 Find the portion α of $\Delta\epsilon$ and Δs , that moves the stress point to the
 1165 intersection with f_M , i_{M1} , (or with f_R , i_{R1}). Note that $\alpha = 0$ means that the
 1166 stress point was already on f_M (or f_R).

1167 Update elastic from i to i_{M1} (or i_{R1}).

1168 Move to *trial 2* with the portion not yet integrated of $\Delta\epsilon$ and Δs given by
 1169 $(1-\alpha)$. At this stage, the stress point is on f_M (or on f_R).

1170 If *trial 1* is outside two yield curves (f_M and f_R).

1171 Find intersection with f_M , α_1 .

1172 Find intersection with f_R , α_2 .

1173 If $\alpha_1 < \alpha_2$ then f_M is reached first.

1174 Update elastic from i to i_{M1} using α_1 .

1175 Move to *trial 2* with $(1-\alpha_1)$. The stress point is on f_M

1176 If $\alpha_2 \leq \alpha_1$ then f_R is reached first.

1177 Elastic update from i to i_{R1} using α_2 (note that if $\alpha_1 = \alpha_2$, then $i_{R1} = i_{M1}$
 1178 and, hence, $\alpha_1 = \alpha_2 = 0$ i.e. stress point is on both f_M and f_R)

1179 Move to *trial 2* with $(1-\alpha_2)$. The stress point is on f_R (if $\alpha_2 < \alpha_1$) or
 1180 on both f_R and f_M (if $\alpha_2 = \alpha_1$).

1181 (B) At this stage, there are three possible ways to compute *trial 2* depending on whether
1182 the stress point is on f_M (point i_{M1} , case B.1) on f_R (point i_{R1} , case B.2) or on both (point
1183 i_Y , case B.3).

1184 (B.1) If the stress point is only on f_M (point i_{M1}) then,

1185 Compute *trial 2* assuming yielding on f_M , but not on f_R (using the portion not yet
1186 integrated of $\Delta\epsilon$ and Δs i.e. $(1-\alpha)$ if *trial 1* crosses only one yield curve or $(1-\alpha_1)$ if *trial*
1187 *1* crosses two yield curves).

1188 If *trial 2* is inside f_R , then yielding on f_M (but not on f_R) has occurred.

1189 Update stress point from i_{M1} to i_{M1+1} assuming yielding on f_M alone (using
1190 $1-\alpha$ or $1-\alpha_1$) and *return*.

1191 If *trial 2* is outside f_R , then *trial 2* crosses f_R at point i_Y , on both f_M and f_R .

1192 Find intersection with f_R $i_R = i_Y$, β . Note that $\beta = 0$ means that the stress
1193 point was already on f_R .

1194 Update stress point from i_{M1} to i_R assuming yielding on f_M alone (using β)
1195 and move to *trial 3*.

1196 At this stage, the stress point is on f_M and f_R (point i_Y). There are only two possible
1197 model responses here: yielding on only f_R or simultaneous yielding on f_M and f_R .
1198 Yielding on only f_M is not possible because, if that was the case, *trial 2* would had fallen
1199 inside f_R when assuming yielding on only f_M and, in fact, the algorithm is at this point
1200 because *trial 2* fell outside f_R .

1201 Compute *trial 3* assuming yielding on f_R (but not on f_M) with $(1-\beta)$.

1202 If *trial 3* is inside f_M , then update the stress point from i_Y to i_{Y+1} assuming
1203 yielding on f_R alone (using $1-\beta$) and *return*.

1204 Otherwise, update the stress point from i_Y to i_{Y+1} assuming simultaneous yielding
1205 on f_M and f_R (using $1-\beta$) and *return*.

1206 (B.2) If the stress point is on f_R (point i_{R1}) then,

1207 Compute *trial 2* assuming yielding on f_R (but not on f_M) using the portion not yet
1208 integrated of $\Delta\epsilon$ and Δs i.e. $(1-\alpha)$ or $(1-\alpha_2)$.

1209 If *trial 2* is inside f_M , then yielding on f_R (but not on f_M) has occurred

1210 Update stress point from i_{R1} to i_{R1+1} assuming yielding on f_R alone (using
1211 $1-\alpha$ or $1-\alpha_2$) and *return*.

1212 If *trial 2* is outside f_M , then *trial 2* crosses f_M at point i_Y , on both f_M and f_R .

1213 Find intersection with f_M $i_M = i_Y$, β .

1214 Update stress point from i_R to i_M assuming yielding on f_R alone (using β)
1215 and move to *trial 3*.

1216 At this stage, the stress point is on f_M and f_R (point i_Y). There are only two possible
1217 model responses here: yielding on only f_M or simultaneous yielding on f_M and f_R . Note
1218 that yielding on only f_R is not possible because, if that was the case, *trial 2* would had
1219 fallen inside f_M when assuming yielding on only f_R and, in fact, fell outside f_M .

1220 Compute *trial 3* assuming yielding on f_M (but not on f_R) with $(1-\beta)$.

1221 If *trial 3* is inside f_R , then update the stress point from i_Y to i_{Y+1} assuming yielding
1222 on f_M alone (using $1-\beta$) and *return*.

1223 Otherwise, update the stress point from i_Y to i_{Y+1} assuming simultaneous yielding
1224 on f_M and f_R (using $1-\beta$) and *return*.

1225 (B.3) If the stress point is on f_M and f_R (point i_Y). There are three possible model
1226 responses here: yielding on only f_R , yielding on only f_M or simultaneous yielding on f_M
1227 and f_R . Therefore, the algorithm may need to compute a maximum of two trials to ensure
1228 the correct model response.

1229 Compute *trial 2* assuming yielding on f_R , (but not on f_M) using the portion not yet
1230 integrated of $\Delta\epsilon$ and Δs i.e. $(1-\alpha)$ or $(1-\alpha_2)$.

1231 If *trial 2* is inside f_M , then yielding on f_R (but not on f_M) has occurred.

1232 Update from i_Y to i_{Y+1} assuming yielding on f_R alone (using $1-\alpha$ or $1-\alpha_2$)
1233 and *return*.

1234 Otherwise, move to *trial 3*.

1235 Compute *trial 3* assuming yielding on f_M (but not on f_R) using the portion not yet
1236 integrated of $\Delta\epsilon$ and Δs i.e. $(1-\alpha)$ or $(1-\alpha_2)$.

1237 If *trial 3* is inside f_R , then update the stress point from i_Y to i_{Y+1} assuming yielding
1238 on f_M alone and *return*.

1239 Otherwise, update the stress point from i_Y to i_{Y+1} assuming simultaneous yielding
1240 on f_M and f_R and *return*.

1241 Note that step (B.3) can be accommodated in steps (B.1) or (B.2), but, for clarification,
1242 it has been kept as a separate case.

1243 8.3 Appendix C

1244 Given the increments of $\Delta\epsilon$ and Δs , the stress state can move from elastic to elasto-
1245 plastic. In the context of the GCM, this means that a *trial* intersects at least one yield
1246 curve and that an intersection point needs to be found. The proposed integration

1247 schemes solve all intersections using the Pegasus algorithm illustrated in Figure C1
1248 (Dowell and Jarratt, 1972). Two conditions are necessary for a *trial* to cross a generic
1249 yield curve f_A . The first one is that the stress point at i is not already lying on f_A
1250 (indicated in Figure C1 as ${}^0f_A < -FTOL$). The second one is that the evaluation of the
1251 yield curve at the *trial* is larger than $FTOL$ (indicated by ${}^1f_A > FTOL$ in Figure C1). If
1252 both of these conditions are true, the Pegasus algorithm finds the scalar α that defines
1253 the portion of $\Delta\epsilon$ and Δs that moves the current stress point to f_A (indicated as i in Figure
1254 C1). A value of $\alpha = 0$ indicates that the initial stress point is already on f_A (i.e. $|f_A| \leq$
1255 $FTOL$) and the update of the stress point is elasto-plastic. A value $\alpha = 1$ indicates that
1256 the final stress point (once the full size of $\Delta\epsilon$ and Δs has been updated) ends up exactly
1257 on f_A so that no intersection occurs. These two extreme cases explain why the possible
1258 values of the scalar α range between 0 and 1.

```

if ( ${}^1f_A > FTOL$ )then      ! ${}^1f_A$  corresponds to  ${}^{trial}f_A$ 
|
| if ( ${}^0f_A < -FTOL$ )then ! ${}^0f_A$  corresponds to  ${}^if_A$ 
| |  $\alpha_0 = 0$ 
| |  $\alpha_1 = 1$ 
| | GO TO 1
| endif
! stress point on  $f_A$  at  $i$ 
 $\alpha = 0$ 
GO TO 3
1 continue
! Find the elastic portion  $\alpha$  of  $(\Delta\epsilon, \Delta s)$  that moves the stress point to  ${}^0f_A$ 
do 2  $n = 1, \text{maxit}$       ! maxit is the maximum number of iterations
|
|  $\alpha = \alpha_1 - (\alpha_1 - \alpha_0) {}^1f_A / ({}^1f_A - {}^0f_A)$ 
|  ${}^t\Delta\epsilon = \alpha\Delta\epsilon$  and  ${}^t\Delta s = \alpha\Delta s$ 
| update with  ${}^t\Delta\epsilon$  and  ${}^t\Delta s$ 
|  $f_A$       ! Evaluation of  $f_A$  at the updated point
| if ( $|f_A| \leq FTOL$ )then
| | GO TO 3
| endif
| if ( ${}^0f_A \cdot f_A > 0$ )then
| |  ${}^1f_A = {}^1f_A \cdot {}^0f_A / ({}^0f_A + f_A)$ 
| else
| |  $\alpha_1 = \alpha_0$ 
| |  ${}^1f_A = {}^0f_A$ 
| endif
|  $\alpha_0 = \alpha$ 
|  ${}^0f_A = f_A$ 
endo
2 continue
STOP      !Algorithm stops (too many iterations)
3 continue
endif

```

1259

1260 Figure C.1 Typical intersection problem using Pegasus algorithm (Dowell and Jarratt,

1261

1972)

1262

1263 9. REFERENCES

- 1264 1. Abbo AJ. Finite element algorithms for elastoplasticity and consolidation. PhD thesis,
1265 University of Newcastle, Australia, (1997).
- 1266 2. Alonso EE, Gens A, Josa A. A constitutive model for partially saturated soils.
1267 *Géotechnique*, 40(3) (1990), pp. 405–430.
- 1268 3. Borja RI, White JA. Continuum deformation and stability analyses of a steep hillside
1269 slope under rainfall infiltration. *Acta Geotech*, 5 (2010), pp. 1–14.
- 1270 4. Cattaneo F, Vecchia GDella, Jommi C. Evaluation of numerical stress-point
1271 algorithms on elastic–plastic models for unsaturated soils with hardening dependent
1272 on the degree of saturation. *Computers and Geotechnics*, 55 (2014), pp. 404–415.
- 1273 5. Dormand JR, Prince PJ. A family of embedded Runge-Kutta formulae. *Journal of*
1274 *Computational and Applied Mathematics*, 6(1) 1980, pp. 19–26.
- 1275 6. Dowell M, Jarratt P. The Pegasus method for computing the root of an equation, *BIT*,
1276 12 (1972), pp. 503–8.
- 1277 7. Gallipoli D, Gens A, Sharma R, Vaunat J. An elasto-plastic model for unsaturated
1278 soil incorporating the effects of suction and degree of saturation on mechanical
1279 behaviour. *Géotechnique*, 53(1) (2003), pp. 123–136.
- 1280 8. Gens A. Soil–environment interactions in geotechnical engineering. *Géotechnique*,
1281 60(1) (2010), pp. 3–74.
- 1282 9. Houlby GT. The work input to an unsaturated granular material. *Géotechnique*, 47(1)
1283 (1997), pp. 193–196.
- 1284 10. Jommi C, Di Prisco C. A simple theoretical approach for modelling the mechanical
1285 behaviour of unsaturated granular soils (in Italian) Il ruolo dei fluidi in ingegneria
1286 geotecnica. *Proc. of Italian conf. Mondovi*, (1994), pp. 167–188.
- 1287 11. Khalili N., Habte M.A., & Zargarbashi S. A fully coupled flow deformation model
1288 for cyclic analysis of unsaturated soils including hydraulic and mechanical hysteresis
1289 *Comp. Geotech.*, 35(6) (2008), pp. 872–889.
- 1290 12. Lloret-Cabot M, Sánchez M, Wheeler SJ. Formulation of a three-dimensional
1291 constitutive model for unsaturated soils incorporating mechanical-water retention
1292 couplings. *International Journal for Numerical and Analytical Methods in*
1293 *Geomechanics*, 37 (2013), pp. 3008–3035.
- 1294 13. Lloret-Cabot M, Sloan SW, Sheng D, Abbo AJ. Error behaviour in explicit
1295 integration algorithms with automatic substepping. *International Journal for*
1296 *Numerical Methods in Engineering*, 108(9) (2016), pp. 1030–1053.

- 1297 14.Lloret-Cabot M, Wheeler SJ, Pineda JA, Romero E, Sheng D. From saturated to
1298 unsaturated conditions and vice versa. *Acta Geotech.*, 13(1) (2018a), pp. 15–37.
- 1299 15.Lloret-Cabot M, Wheeler SJ, Pineda JA, Romero E, Sheng D. Reply to Discussion
1300 of “From saturated to unsaturated conditions and vice versa”. *Acta Geotech.*, 13(2)
1301 (2018b), pp. 493–495.
- 1302 16.Lloret-Cabot M, Wheeler SJ, Sánchez M. A unified mechanical and retention model
1303 for saturated and unsaturated soil behaviour. *Acta Geotech.*, 12(1) (2017), pp. 1–
1304 21.
- 1305 17.Lloret-Cabot M, Wheeler SJ, Sánchez M. Unification of plastic compression in a
1306 coupled mechanical and water retention model for unsaturated soils. *Can. Geotech.*
1307 *J.*, 51(12) (2014), pp. 1488–1493.
- 1308 18.Lloret-Cabot M, Wheeler, SJ. The mechanical yield stress in unsaturated and
1309 saturated soils. *Proc. 7th Int. conf. unsat. soils* (eds W.W. Ng, A.K. Leung, A.C.F.
1310 Chiu, C. Zhou), Hong Kong, HKUST, (2018), pp. 221-226.
- 1311 19.Ng CWW, Pang, YW. Influence of stress state on soil-water characteristics and
1312 slope stability. *J. Geotech. Eng. ASCE*, 126(2) (2000), pp. 157–166.
- 1313 20.Nuth M. Laloui L. Advances in modelling hysteretic water retention curve in
1314 deformable soils. *Comp. Geotech.*, 35(6) (2008), 835–844.
- 1315 21. Olivella S, Gens A, Carrera J, Alonso EE. Numerical formulation for a simulator
1316 (CODE_BRIGHT) for the coupled analysis of saline media. *Engineering*
1317 *Computations*, 13(7): (1996), pp. 87–112.
- 1318 22.Pedroso DM, Sheng D, Sloan, SW. Stress update algorithm for elastoplastic models
1319 with nonconvex yield surfaces. *International Journal for Numerical Methods in*
1320 *Engineering*, 76 (2008), pp. 2029–2062.
- 1321 23.Pérez-Foguet A, Rodríguez-Ferran A, Huerta A. Consistent tangent matrices for
1322 substepping schemes, *Computer Methods in Applied Mechanics and Engineering*,
1323 190(35-36) (2001), pp. 4627–4647.
- 1324 24. Pinyol NM, Alonso EE, Olivella, S. Rapid drawdown in slopes and embankments.
1325 *Water Resources Research*, 44(5) 2008, pp. 1–22.
- 1326 25.Potts DM, Gens A. A critical assessment of methods of correcting for drift from the
1327 yield surface in elastoplastic finite element analysis. *International Journal for*
1328 *Numerical and Analytical Methods in Geomechanics*, 9 (1985), pp. 149–59.

- 1329 26.Potts DM, Gens A. The effect of the plastic potential in boundary value problems
1330 involving plane strain deformation. *International Journal for Numerical and*
1331 *Analytical Methods in Geomechanics*, 8(3) (1984), 259–286.
- 1332 27. Potts DM, Zdravkovic L. *Finite element analysis in geotechnical engineering:*
1333 *theory*, (1999). Thomas Telford, London.
- 1334 28.Romero E, Gens A, Lloret A. Water permeability, water retention and
1335 microstructure of unsaturated compacted Boom clay. *Eng. Geol.*, 54 (1999), pp.
1336 117–127.
- 1337 29.Roscoe KH, Burland JB. On the generalised stress-strain behavior of wet clay.
1338 *Engineering Plasticity* (eds Heyman J & Leckie FA), Cambridge University Press,
1339 Cambridge, (1968), pp. 535–609.
- 1340 30.Sánchez M, Gens A, Guimarães L, Olivella S. Implementation algorithm of a
1341 generalised plasticity model for swelling clays. *Computers Geotechnics*, 35(6)
1342 (2008), pp. 860–871.
- 1343 31.Shampine LF. *Numerical Solution of Ordinary Differential Equations*. Chapman &
1344 Hall, London, (1994).
- 1345 32. Sheng D, Sloan SW, Gens A, Smith DW. Finite element formulation and algorithms
1346 for unsaturated soils. Part I: Theory. *International Journal for Numerical and*
1347 *Analytical Methods in Geomechanics*, 27 (2003a), pp. 745–765.
- 1348 33. Sheng D, Sloan SW, Gens A, Smith DW. Finite element formulation and algorithms
1349 for unsaturated soils. Part II: Verification and Application. *International Journal for*
1350 *Numerical and Analytical Methods in Geomechanics*, 27 (2003b), pp. 767–790.
- 1351 34.Sheng D, Sloan SW, Yu HS. Aspects of finite element implementation of critical
1352 state models. *Computational mechanics*, 26 (2002), pp. 185–196.
- 1353 35.Sloan SW, Abbo AJ, Sheng D. Refined explicit integration of elastoplastic models
1354 with automatic error control. *Engineering Computations*, 18(1-2) (2001), pp. 121-
1355 154. Erratum: *Engineering Computations*, 19(5-6) (2002), pp. 594–594.
- 1356 36.Sloan SW. Substepping schemes for the numerical integration of elastoplastic stress-
1357 strain relations. *International Journal for Numerical Methods in Engineering*, 24
1358 (1987), pp. 893–911.
- 1359 37.Sołowski WT, Gallipoli D. Explicit stress integration with error control for the
1360 Barcelona Basic Model. Part I: Algorithms formulations. *Computers and*
1361 *Geotechnics*, 37(1-2) (2010a), pp. 59–67.

- 1362 38. Sołowski WT, Gallipoli D. Explicit stress integration with error control for the
1363 Barcelona Basic Model. Part II: Algorithms efficiency and accuracy. *Computers and*
1364 *Geotechnics*, 37(1-2) (2010b), pp. 68–81.
- 1365 39. Sołowski WT, Sloan SW. Elastic or Elasto-Plastic: Examination of Certain Strain
1366 Increments in the Barcelona Basic Model. *Proc. 2nd Eur. conf. unsat. soils* (eds C
1367 Mancuso, C Jommi, F D'Onza), Naples, (2012), Springer, pp. 85-91.
- 1368 40. Sołowski WT, Hofmann M, Hofstetter G, Sheng D, Sloan S. A comparative study
1369 of stress integration methods for the Barcelona Basic Model. *Computers and*
1370 *Geotechnics*, 44 (2012), pp. 22–33
- 1371 41. Tarantino A. A water retention model for deformable soils. *Géotechnique*, 59(9)
1372 (2009), pp. 751–762.
- 1373 42. Tsiamposi A, Zdravkovic L, Potts DM. Variation with time of the factor of safety
1374 of slopes excavated in unsaturated soils *Computers and Geotechnics*, 48(2) (2013),
1375 pp. 167–178.
- 1376 43. Wheeler SJ, Sharma RS, Buisson MSR. Coupling of hydraulic hysteresis and stress–
1377 strain behaviour in unsaturated soils. *Géotechnique*, 53(1) (2003), pp. 41–54.
- 1378 44. Zhao J, Sheng D, Rouainia M, Sloan SW. Explicit stress integration of complex soil
1379 models. *International Journal for Numerical and Analytical Methods in*
1380 *Geomechanics*, 29 (2005), pp. 1209–1229.
- 1381 45. Zhang Y, Zhou AN. Explicit integration of a porosity-dependent hydro-mechanical
1382 model for unsaturated soils. *Int J Numer Anal Meth Geomech*, 40 (2016), pp. 2353-
1383 2382.
- 1384 46. Zhang Y, Zhou AN, Nazem M, Carter J. Finite element implementation of a fully
1385 coupled hydro-mechanical model and unsaturated soil analysis under hydraulic and
1386 mechanical loads. *Computers and Geotechnics*, 110 (2019), pp. 222–241.
- 1387 47. Zhou AN, Sheng D. An advanced hydro-mechanical constitutive model for
1388 unsaturated soils with different initial densities. *Computers and Geotechnics*, 63
1389 (2015), pp. 44–66.